Gravitational Lensing of Gravitational Wave Packets

Rahul Ramesh

A dissertation submitted for the partial fulfilment of BS-MS dual degree in Science

Indian Institute of Science Education and Research, Mohali

April 2021

Certificate of Examination

This is to certify that the dissertation titled **Gravitational Lensing of Gravitational Wave Packets** submitted by **Rahul Ramesh** (Reg. No. MS16036) for the partial fulfillment of BS- MS Dual Degree programme of the institute, has been examined by the thesis committee duly appointed by the institute. The committee finds the work done by the candidate satisfactory and recommends that the report be accepted.

Dr. Ambresh Shivaji Dr. Harvinder K. Jassal Prof. Kulinder P. Singh

Prof. Jasjeet S. Bagla
(Supervisor)

Dated: April 28, 2021

Declaration

The work presented in this dissertation has been carried out by me under the guidance of Prof. Jasjeet Singh Bagla at the Indian Institute of Science Education and Research, Mohali.

This work has not been submitted in part or in full for a degree, a diploma, or a fellowship to any other university or institute. Whenever contributions of others are involved, every effort is made to indicate this clearly, with due acknowledgement of collaborative research and discussions. This thesis is a bonafide record of original work done by me and all sources listed within have been detailed in the bibliography.

Rahul Ramesh
(Candidate)
Dated: April 28, 2021

In my capacity as the supervisor of the candidates project work, I certify that the above statements by the candidate are true to the best of my knowledge.

Prof. Jasjeet Singh Bagla
(Supervisor)
Dated: April 28, 2021

Acknowledgements

I would like to begin by thanking my supervisor, Prof. Jasjeet Singh Bagla, for his constant guidance and motivation over the last five years of my stay at IISER-Mohali. In addition to supervising this MS Thesis, he had given me an opportunity to work with him during my first year on a project on Galactic Rotation. Although no new results emerged as part of this study, this experience gave me an initial feel of what research involves, and I undoubtedly believe that this has served as a strong foundation for everything that I've learned since. He has also been my local guide for the summer projects that I've undertaken outside IISER, and I would like to thank him for the interactions that we've had with respect to this. With regards to this MS Thesis, I would also like to thank Ashish Meena for all discussions and comments from his side.

While the academic year of 2020-21 has been an unfortunate one for almost all students and researchers, I feel that the graduating batch of 2021 is amongst the unluckiest. In response to protocols drawn up to counter the COVID-19 pandemic, most of us were away from campus for a majority of this year – the year that maybe our last on this beautiful campus and amongst this amazing set of fellow students and researchers. In these rather ill-fated times, I would like to thank my friends – Abhijit, Anshuman and Rishi, in particular – for all those virtual chats throughout the lockdown period and beyond. This truly gave me the 'campus experience' while staying away from campus.

This section will forever remain incomplete unless I thank my family. A heartful thank you to my parents and grand-parents, who have encouraged me throughout these 23 years of my life. Everything that I ever achieve will always be dedicated to them.

List of Figures

Abstract

The recent observation of GW150914 has led to the birth of a new field: Gravitational Wave Astronomy. With three currently active detectors, and a few more scheduled to be operational within the next decade or so, the relevance of this field is expected to vastly increase. Akin to electromagnetic radiation, the propagation of gravitational radiation is affected by local changes in the curvature of space-time. However, there is one crucial difference: the wavelength of gravitational waves that are of astrophysical interest are much larger than that of light, and hence wave effects may become important in some instances. In particular, wave effects cannot be ignored if the wavelength of radiation is comparable to the physical size of the gravitational lens. Unlike in the geometric optics regime where all frequency components are magnified by the same factor, wave effects introduce frequency dependent modulation.

Based on the length of the signal in time domain, gravitational wave signals can be broadly classified into two types: signals can run for long periods of time, like the gravitational wave signal produced during the in-spiral of two massive objects, or continuous gravitational waves produced by, for e.g., a rotating neutron star with an irregularity on its surface. As opposed to this, gravitational wave packets are short bursts of gravitational radiation, and as per current understanding, these do not exceed a time-length of one second. Another key difference is that the chirp signal is quasi-monochromatic, while the wave packets under consideration are not. In this MS thesis, we have aimed to study, and quantify, the distortions that can be induced in a gravitational wave packet as a result of gravitational lensing.

For frequencies in the LIGO-band, wave effects are only important in the case of microlensing. We have thus focused on the microlensing of gravitational wave packets. To connect with observations, we have simulated wave packets that are similar to those produced during core-collapse supernovae. We hope that the results of this thesis will find applications in the future, when increased sensitivity of detectors will allow detection of multiple instances of lensed gravitational wave packets.

Contents

Chapter 1

Introduction

When Albert Einstein published his General Theory of Relativity (GTR) in 1916, it brought about a radical change in the understanding of physics. However, this was only a theory, and there was no available observational evidence to support it at that time. Since then, this grand theory has undergone multiple observational 'tests', and these observations have all but confirmed its authenticity. In this thesis, (a combination of) two of these 'tests' will be discussed: Gravitational Lensing and Gravitational Waves.

Gravitational Lensing was first observed about a century ago, by Sir Arthur Eddington in 1919. He made use of a Total Solar Eclipse to record the position of stars in the Hyades Cluster, which wouldn't otherwise be visible at that time of the day owing to the brightness of the Sun. These measurements pointed towards the fact that the 'apparent' position of the stars had changed: the incoming photons from these stars were deflected by the Gravitational Lens (aka the Sun) that was present in their path. This observation not only confirmed Einstein's prediction of Gravitational Lensing, but also disproved the Lensing theory derived using Newtonian Gravity, which predicted a deflection angle that was off by a factor of two.

Another prediction of the GTR was the existence of Gravitational Waves: ripples of space-time that propagate at the speed of light. These waves (alternatively) squeeze and stretch any object (or even empty space) that they pass through. At astronomical/cosmological distances from the source, the strain produced is usually of the order of 10^{-19} (the corresponding change in length for the LIGO arm would be around the width of a proton) or even smaller, which is impossible to measure using any 'standard' ruler. To overcome this limitation, the idea of using laser interferometers was put forward: since space itself is stretched/squeezed as gravitational waves pass through, there would be a change in the interference pattern produced by the interferometer. The idea was to use this change to measure the strain produced. As good as the idea sounds, there were a fair share of technological issues/limitations involved. After numerous efforts, gravitational waves were

finally discovered directly for the first time in 2015 by the LIGO and VIRGO collaboration ([Collaboration 16]). This 'chirp signal' was emitted as a result of a Binary Black Hole merger that took place over a billion years ago. Since then, over fifty more instances of such events have been observed, and this ever growing field promises to provide an exciting tool to probe the universe.

In addition to the chirp signal produced during the merger of two massive objects, gravitational waves are also emitted during Core-Collapse Supernovae (CCSNe) events. Although these haven't yet been detected by the LIGO/VIRGO interferometers, various computer simulations have yielded a multitude of information about such signals (for e.g: [Andresen 17], [Powell 20], [Vartanyan 20]): the signal maintains high intensity for a period of around 0.5 to 1 second following the bounce, with the frequency ranging between a few Hertz to a thousand Hertz. Different frequency components are produced by different processes – f-mode oscillations of the proto-neutron star are responsible for the high frequency components, asymmetrical neutrino/matter emissions produce waves at the lower end of the frequency domain, while prompt convection and the Standing Accretion Shock Instability (SASI) account for intermediate frequencies. When detected, these signals thus have the potential to offer a multidimensional probe into CCSNe events.

As gravitational waves propagate towards the Earth, they may encounter gravitational lenses along the way. The lensing that takes place is similar to what happens in the case of electromagnetic radiation, but with one important difference: the wavelength of gravitational waves is much larger than their electromagnetic counterpart, and in some cases, wave optics may be required to describe their propagation. Figure 1.1, which is a plot of Frequency of Radiation 'f' versus Mass of the Gravitational Lens 'M_L', provides a crude idea of when wave optics may need to be considered: the line running diagonally across the plot is the regime where wave effects are non-negligible. To the far right of this line, propagation may be described by geometric optics. To the far left, the wavelength is be so large that lensing would be absent. The shaded blue region represents the band that is currently active – the LIGO/VIRGO band. Within this frequency range, only micro-lenses ($\sim 10M_\odot < M_L < \sim 100M_\odot$) are important from the perspective of wave optics.

As discussed in Chapter 2, lensing is achromatic once wave effects are non-negligible. As a result, the lensed signal may appear very different in comparison to the original one. A lensed signal may thus 'dilute' the information that could possibly be gleaned. It is therefore important to identify such lensed signals, and if possible, de-lens them.

At the moment, there are no available templates to faithfully reproduce CCSNe signals. Thus, it is not a straightforward task to identify whether a signal has been lensed or not. In this thesis, we have aimed to explore this challenge, and develop a possible statistical technique that can be employed. The rest of the thesis is organised as follows: In Chapter

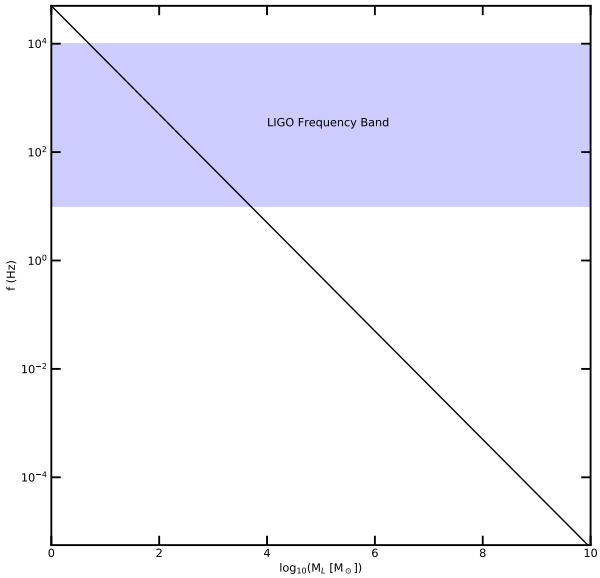

Figure 1.1: A plot of Frequency of Radiation 'f' versus Mass of the Gravitational Lens 'M_L'. The region immediately surrounding the diagonal line is where wave effects are important.

2, we review the formalism of Wave Optics in Gravitational Lensing. As will be explained in detail later on, this chapter assumes that the lens system can be approximated by a *single* lens plane. This of course is not a very general scenario. Chapter 3 expands the formalism to a slightly more general case, wherein the lens system can lie along N-different planes. In Chapter 4, we discuss the lensing of CCSNe signals, and their possible identification. We summarise the thesis in Chapter 5, and mention auxiliary information in the Appendix. Although our work is aimed towards gravitational waves produced during CCSNe, the physics and methods employed can be used for gravitational waves emitted in any possible way.

Chapter 2

Wave Effects in Gravitational Lensing

In this Chapter, we begin by reviewing the basics of gravitational lensing in the geometric optics regime ([Narayan 96]). We next provide a brief overview of the physics involved when wave effects become non-negligible in the case of gravitational lensing of gravitational waves ([Misner 73], [Schneider 92], [Nakamura 99]). The formalism of wave optics is the most fundamental, and as we show, the equation in case of geometric optics can be derived as a limit of wave optics. In the later part of this chapter, we explore the typical behavior of various lens systems.

2.1 Basics of Gravitational Lensing

In this section, we explore the basics of Gravitational Lensing as described in the geometric optics regime. The simplest approach to gravitational lensing is to assume a locally flat spacetime which is perturbed by a distribution of matter. This condition is satisfied as long as the (dimensionless) gravitational potential is small ($U(=\phi/c^2) \ll 1$), and the peculiar velocity of the lens is small ($v_p \ll c$). Provided the preceding assumptions hold, the effective refractive index is given by ([Schneider 92]):

$$n = 1 - 2U = 1 + 2|U| \tag{2.1}$$

Due to the increased refractive index ($n > 1$), the radiation slows down:

$$v = \frac{c}{n} \sim c - 2|U|c \tag{2.2}$$

This reduced speed gives rise to a time delay that is commonly referred to as the Shapiro delay ([Shapiro 64]):

$$t_{\text{shap}} = \int \frac{2|U|}{c} dl \tag{2.3}$$

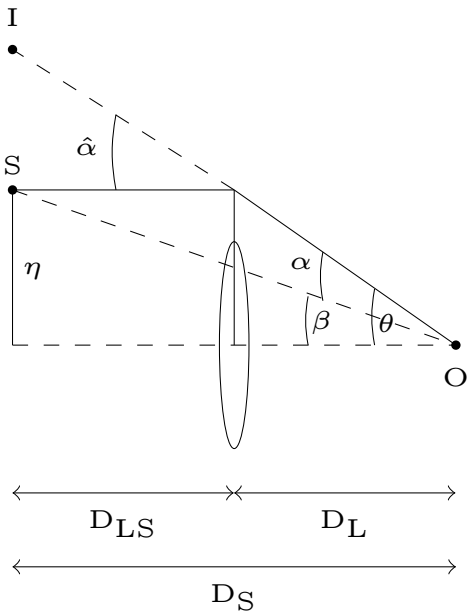

Figure 2.1: A typical lens configuration. The gravitational lens deflects the incoming radiation from a source at position β, due to which an observer observes the corresponding image at an angular position θ.

Akin to on optical lens, a gravitational lens also deflects any radiation that passes close to it. The deflection angle is given by:

$$\hat{\alpha} = 2 \int \vec{\nabla}_{\perp} U dl \tag{2.4}$$

The above two integrals are performed along the path followed by the radiation as it propagates from the source to the observer.

A typical lens configuration is depicted in Figure 2.1. The distance between the observer and the source (lens) is D_S (D_L), while the distance between the lens and source is D_{LS}. Note that these distances are angular diameter distances. The source is present at an angular position β. Due to gravitational lensing, the incoming radiation is deflected by an angle $\hat{\alpha}$, and the apparent angular position of the source is θ. From Figure 2.1, we see that $\theta D_S = \beta D_S + \hat{\alpha} D_{LS}$. By defining a reduced deflection angle $\alpha = (D_{LS}/D_S)\ \hat{\alpha}$, one obtains the following relation:

$$\beta = \theta - \alpha(\theta) \tag{2.5}$$

This is called the ray-tracing equation or the lens equation. For a given source position β, one can use this equation to obtain the positions of the various images that are formed.

2.2 Gravitational Waves and their Propagation

The gravitational wave is viewed as a tensor perturbation to the background metric:

$$ds^2 = -(1+2U)\,dt^2 + a^2(1-2U)\,d\mathbf{r}^2 = g^{(B)}_{\mu\nu}dx^\mu dx^\nu \tag{2.6}$$

$$g_{\mu\nu} = g^{(B)}_{\mu\nu} + h_{\mu\nu} \tag{2.7}$$

Here, $g^{(B)}_{\mu\nu}$ is the background metric, $g_{\mu\nu}$ is the altered metric of space-time when a gravitational wave $h_{\mu\nu}$ propagates through it, and U is the (dimensionless) gravitational potential. The gravitational wave can be expressed in terms of a scalar (ϕ) and a polarisation tensor ($e_{\mu\nu}$) ([Baraldo 99]):

$$h_{\mu\nu} = \phi e_{\mu\nu} \tag{2.8}$$

As the gravitational wave propagates forward in space-time, the polarization tensor is parallel transported along the null geodesic, and the change in $e_{\mu\nu}$ is negligible as long as $U \ll 1$. In this limit, the propagation of the gravitational wave can be described solely in terms of the scalar ϕ, and the wave equation in frequency domain is given by:

$$\left(\nabla^2 + \widetilde{\omega}^2\right)\widetilde{\phi} = 4\widetilde{\omega}^2 U\widetilde{\phi} \tag{2.9}$$

To understand the propagation of the wave, one needs to solve Equation (2.9). In general, the incoming wavefront would require a three-dimensional treatment. However, as long as the distances between the source, lens and observer are large compared to the physical spread of the lens system, one can assume the 'Thin Lens Approximation': the lens system is assumed to be planar. Under this approximation, the underlying calculations reduce to a two-dimensional problem. In this chapter, we assume that all the lens systems are confined to a single lens plane. We later generalise this to 'N' lens planes in Chapter 3.

Figure 2.2 outlines the assumed lens configuration: The source and the lens systems are confined to the source and lens plane respectively, which are at distances $\mathrm{D_S}$ and $\mathrm{D_L}$ from the observer. The distance between the source and lens plane is denoted by $\mathrm{D_{LS}}$. The position of the source on the source plane is given by η, and vectors on the lens plane are denoted by ξ.

The propagation of the incoming wavefront across the lens plane can be evaluated using the Kirchhoff Diffraction Integral ([Schneider 92]) (or using the Path Integral Formalism [Nakamura 99]). The lensed wave is commonly represented in terms of the Amplification Factor, which is the ratio between the scalars of the lensed and unlensed waves:

$$F(f,\eta) = \frac{\widetilde{\phi}^L_{obs}}{\widetilde{\phi}_{obs}} = \frac{D_S}{D_L D_{LS}}\frac{f(1+z_L)}{i}\int d^2\xi\, \exp\left[2\pi i f(1+z_L)t_d(\xi,\eta)\right] \tag{2.10}$$

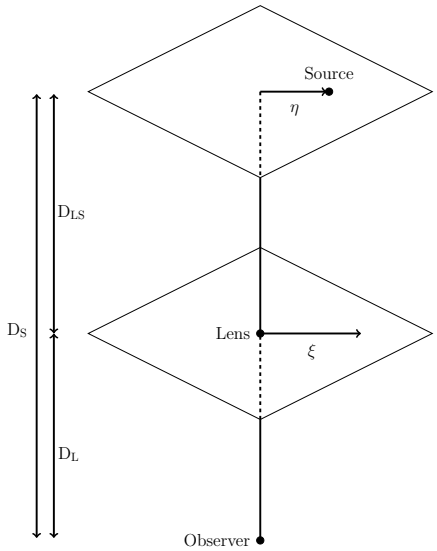

Figure 2.2: Gravitational Lens Configuration. We assume the so called 'Thin-Lens Approximation', and also assume that all lenses are confined to a single lens plane. All symbols carry their usual meaning as elaborated in the main text.

In the above equation, z_L is the redshift of the lens, and the various distances – D_S, D_L and D_{LS} – are angular diameter distances. The term $t_d(\xi,\eta)$ is called the time delay function, and is given by:

$$t_d(\xi,\eta) = \frac{D_L D_S}{2D_{LS}}\left(\frac{\xi}{D_L} - \frac{\eta}{D_S}\right)^2 - \psi(\xi) + \phi(\eta) = \mathrm{t_{geom}} + \mathrm{t_{grav}} + \mathrm{t_{arr}} \tag{2.11}$$

The term $\psi(\xi)\left(=\frac{2D_{LS}}{D_L D_S}\int dz\, U(\xi,z)\right)$ is called the lensing potential, and is the Newtonian potential of the lens systems integrated along the line of sight. It can be visualised as the potential projected onto the lens plane. The three terms in Equation (2.11) correspond to three different physical quantities: $\mathrm{t_{geom}}$ is the time delay caused by the extra geometric distance that the wave has to travel due to the presence of the lens, $\mathrm{t_{grav}}$ is identical to the Shapiro delay discussed earlier (but with an additional scaling factor), and $\mathrm{t_{arr}}$ is the time taken by the unlensed wave to reach the observer. The last term only contributes a phase difference to the amplification factor, and is often assigned a value such that the time delay of the first image (corresponding to the global minima of the time delay function) is zero.

For ease of computation, it is often convenient to rewrite the above equations in terms of dimensionless quantities: the two vectors ξ and η are normalised by an arbitrary length scale ξ_0:

$$\mathbf{x} = \frac{\xi}{\xi_0}$$

$$\mathbf{y} = \frac{\eta D_L}{\xi_0 D_S}$$

The dimensionless frequency and the dimensionless time delay function are given in terms of $\mathbf{x}$ and $\mathbf{y}$ as:

$$\omega = \frac{D_S}{D_{LS} D_L} 2\pi \xi_0^2 (1+z_L) f$$

$$t_d(\mathbf{x},\mathbf{y}) = \frac{1}{2}|\mathbf{x}-\mathbf{y}|^2 - \psi(\mathbf{x}) + \phi(y)$$

where, $\psi(\mathbf{x}) = D_{LS} D_L / (\xi_0^2 D_S)\psi(\xi)$ and $\phi(\mathbf{y}) = D_{LS} D_L / (\xi_0^2 D_S)\phi(\eta)$. Equation (2.10) is re-written in terms of these dimensionless quantities as:

$$F(\omega, y) = \frac{\omega}{2\pi i} \int d^2\mathbf{x} \exp\left[i\omega t_d(\mathbf{x},\mathbf{y})\right] \tag{2.12}$$

Due to the highly oscillatory nature of the above integrand, when $\omega t_d(\mathbf{x},\mathbf{y}) \gg 1$, only stationary points contribute to the integral. A stationary point could either correspond to a minima, saddle point or maxima of the time delay function. In gravitational lensing, the images corresponding to these points are referred to as Type-I, Type-II and Type-III images respectively. In this limit, Equation (2.12) reduces to ([Nakamura 99]):

$$F_{\text{geom}}(\omega, \mathbf{y}) = \sum_j \sqrt{|\mu_j|} \exp\left(i\omega t_{d,j} - i\pi n_j\right) \tag{2.13}$$

where, μ_j corresponds to the magnification of the j^{th} image. n_j is the Morse index, which is equal to the number of negative eigenvalues of the Hessian of the j^{th} image, and equals 0, 1/2 and 1 for a Type-I, -II and -III image respectively. Thus, a Type-I, -II and -III image would be out of phase with respect to the original signal by 0, $\pi/2$ and π respectively. Note that this phase difference is in addition to that induced by the geometric and gravitational time delays. Under almost all scenarios, the frequency of electromagnetic waves is so large that no oscillations are observed in the amplification factor. One notable exception is the case of femtolensing of gamma-ray bursts (for e.g. [Ulmer 95]). Although this scenario has been of theoretical interest, it hasn't yet been observed.

2.3 Examples of Lens Models

In this section, we describe possible lens models and the corresponding amplification factors. We always assume that the lens can be approximated by a point mass object. For microlenses, this approximation is valid under most relevant astrophysical scenarios, more about which is mentioned in Appendix A.

2.3.1 Isolated Point Mass Lens

The simplest lens model is that of an Isolated Point Mass Lens. For the choice of $\xi_0 = \sqrt{4GM_L D_L D_{LS}/c^2 D_S}$, the Lensing Potential for such a lens is $\psi(\mathbf{x}) = \ln(|\mathbf{x}|)$. The term M_L stands for the mass of the lens, and the choice of ξ_0 is called the Einstein Radius. This is the radius of the 'ring' that is formed in the strong lensing regime when the source, lens and observer happen to be collinear. For this lens system, Equation (2.12) can be integrated analytically to obtain ([Peters 74]):

$$\begin{aligned} F(\omega, y) &= \exp\left[\frac{\pi\omega}{4} + \frac{i\omega}{2}\left\{\ln\left(\frac{\omega}{2}\right) - 2\phi_m(\mathbf{y})\right\}\right] \\ &\quad \Gamma\left(1 - \frac{i\omega}{2}\right) {}_1F_1\left(\frac{i\omega}{2}, 1; \frac{i\omega}{2} y^2\right) \end{aligned} \tag{2.14}$$

where, $\omega = 8\pi G(1+z_L)M_L f/c^3$, $\phi_m(\mathbf{y}) = (\mathbf{x_m} - \mathbf{y})^2/2 - \ln x_m$ with $x_m = \left(y + \sqrt{y^2+4}\right)/2$, and ${}_1F_1$ is the hypergeometric function. An Isolated Point Mass produces two images with a time delay of $\Delta t = \frac{y\sqrt{y^2+4}}{2} + \ln\left(\frac{\sqrt{y^2+4}+y}{\sqrt{y^2+4}-y}\right)$, with magnifications $\mu_\pm = \frac{1}{2} \pm \frac{y^2+2}{2y\sqrt{y^2+4}}$. Using Equation (2.13), the geometric optics limit ($\omega \gg 1$) of Equation (2.14) is given by:

$$F_{\text{geom}}(\omega, \mathbf{y}) = \sqrt{|\mu_+|} - i\sqrt{|\mu_-|}\exp(i\omega\Delta t) \tag{2.15}$$

Figure 2.3 portrays the difference between what one would obtain using geometric optics (in black) as opposed to the complete wave optics calculation (blue). The source is positioned at $\mathbf{y}$ = (1,0), and the mass of the lens is taken to be $50M_\odot$. At low frequencies ($f \lesssim 600$Hz), there are visible differences between the two curves. This difference arises due to diffraction. The oscillatory nature of the amplification factor arises as a result of the superposition between the two (time-separated) images.

The amplification factor is a function of ω, or equivalently f, and $y = |\mathbf{y}|$. The left panel of Figure 2.4 shows |F| as a function of f for different values of y (all for M_L = $50M_\odot$) – As one transitions from a higher to lower value of y, two qualitative differences take place: the peak value of the amplification factor increases (corresponding to an increase in magnification of the images), and oscillations become less rapid (due to a decrease in time-delay between images). For instance, the black curve ($y = 3$) oscillates more rapidly in comparison to the red curve ($y = 0.2$), but the range of oscillations is smaller.

For a fixed value of y, since $\omega \propto M_L$, the rate of oscillation of |F| increases with the mass of the lens. The right panel of Figure 2.4 shows this for a value of $y = 1$. For example, the range of oscillation of the blue (M_L = $50M_\odot$) and red (M_L = $100M_\odot$) curves is the same, but the red curve oscillates about twice as fast.

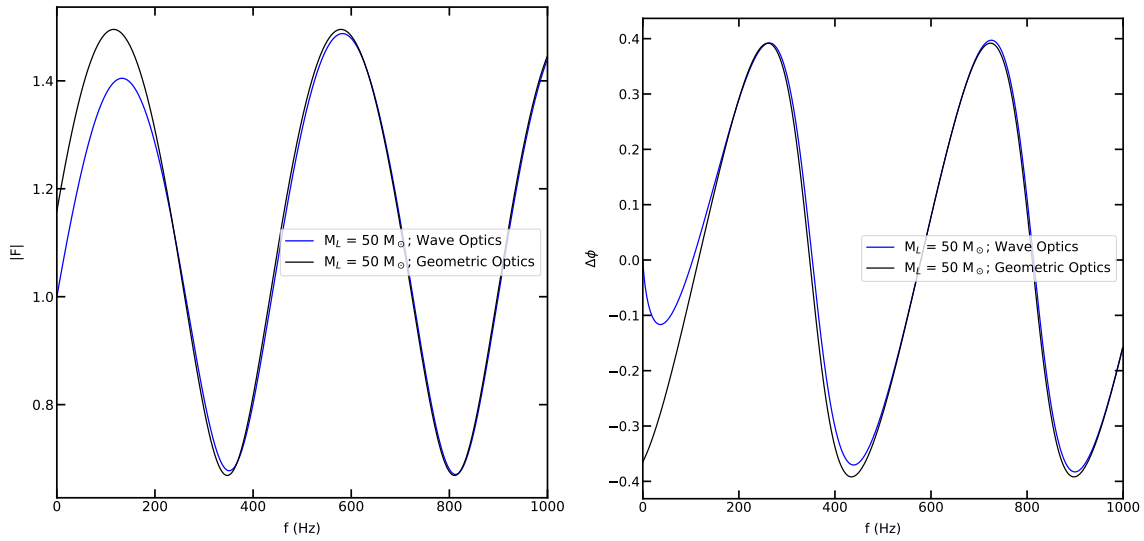

Figure 2.3: Comparison between Amplification Factors obtained using Geometric Optics (black) versus the complete Wave Optics Calculation (blue). The lens is assumed to be a $50M_{\odot}$ Isolated Point Mass Lens, with the source postioned at $\mathbf{y} = (1,0)$. The left panel plots the modulus, while the phase $\Delta\phi = -i\ln(F/|F|)$ is shown in the right panel.

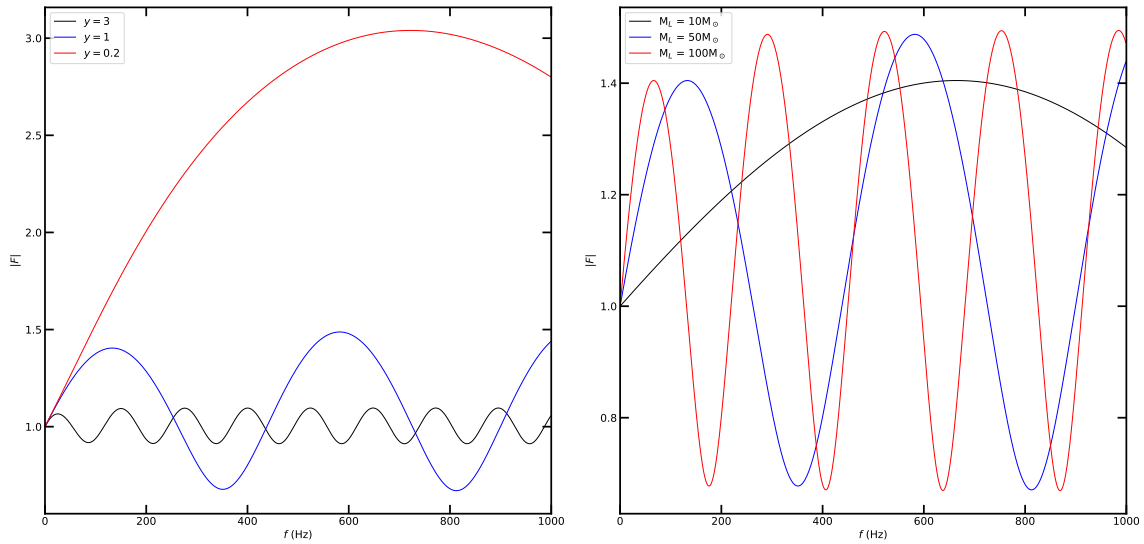

Figure 2.4: Qualitative Dependence of |F| on $|\mathbf{y}|$ and M_L. In the left panel, $M_L = 50M_{\odot}$, while the value of $|\mathbf{y}|$ is varied. The right panel assumes a constant value of $|\mathbf{y}|$, while the value of M_L is varied.

2.3.2 Point Mass Lens Embedded in a Galaxy Potential

While the Isolated Point Mass Lens model provides initial insights into the behaviour of the amplification factor, it is not a very realistic model. One step towards more realistic lensing scenarios is to consider a model where a Point Mass Lens is embedded in a galaxy. In what follows, we model the galaxy as a cored isothermal ellipsoid. Due to the small size of the micro-lens, the effect of the galaxy can be assumed to be constant across the size of the micro-lens. Under this assumption, the galaxy alters the lensing potential of the micro-lens by contributing two terms: external convergence (κ), and shear (γ_1, γ_2). The effect of the former is to enlarge/minimize the image in an isotropic fashion, while shear distorts the image unequally in different directions. Note that this description is more intuitive when one deals with electromagnetic radiation where 'actual' images can be seen, as opposed to the strain that is observed in case of gravitational waves. The lensing potential of a point mass lens embedded in a galaxy is given by ([Schneider 92]):

$$\psi(x_1, x_2) = \ln\left(\sqrt{x_1^2 + x_2^2}\right) + \frac{\kappa}{2}(x_1^2 + x_2^2) + \frac{\gamma_1}{2}(x_1^2 - x_2^2) + \gamma_2 x_1 x_2 \tag{2.16}$$

No analytic solution is available for such a lens system, and hence one has to integrate Equation (2.12) numerically to obtain the amplification factor. While it is possible to directly evaluate the integral in frequency-domain, the Ulmer-Goodman formalism ([Ulmer 95]) provides a faster approach to compute the integral in time-domain. Throughout the rest of this section, we have used the latter to evaluate the respective amplification factors. A more detailed note on this method is provided in Appendix B.

Figure 2.5 highlights the features that external strong lensing induces into the amplification factor of a point mass lens: On the left panel, different values of $(\kappa, \gamma_1, \gamma_2)$ are assumed, all for a source positioned at $y = 1$. For small values of $(\kappa, \gamma_1, \gamma_2)$, as has been assumed in this figure, both convergence and shear increase the time delay between images, which results in the amplification factor oscillating faster than the isolated point mass lens counterpart. The difference is that convergence increases the values of |F|, while shear decreases it.

Even with external convergence, the number of images for a single point mass lens is restricted to two. However, in the presence of external shear, this number can increase to four, depending on the position of the source – for sources within the caustic, four images are formed, and two images otherwise. On the right panel of Figure 2.5, we show the amplification factor for a case where four images are formed ($\mathbf{y} = (0.1, 0.1)$). For reference, the amplification factor for an isolated point mass for the same value of y is shown in black. In addition to faster oscillations of the blue curve, one can notice richer patterns in the amplification factor formed as a result of the interference between the four images.

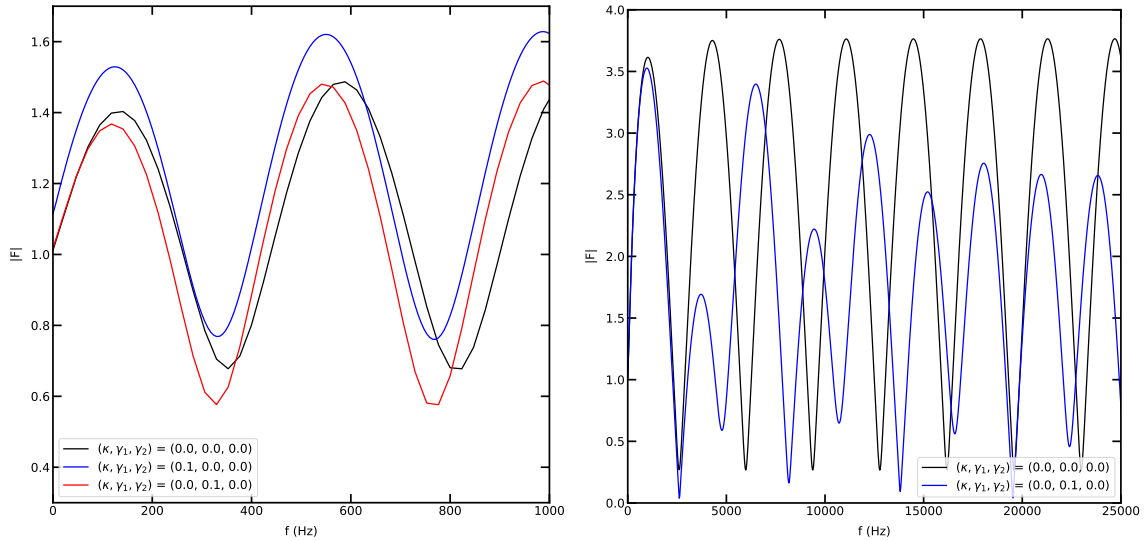

Figure 2.5: Effect of external convergence and shear on the amplification factor of a point mass lens.

2.3.3 'N' Point Mass Lenses on a Single Lens Plane

Until now, we have assumed that there is only one micro-lens situated on the lens plane. In a more general case, we could have 'N' Point Mass Lenses spread across the Lens Plane. If the i^{th} lens has a mass of M_i, and is positioned at $\mathbf{l_i}$ on the lens plane, the lensing potential is given by ([Asada 09]):

$$\psi(\mathbf{x}) = \Sigma_i m_i \ln(|\mathbf{x} - \mathbf{l_i}|) \tag{2.17}$$

where, $m_i = \frac{M_i}{\Sigma_i M_i}$ is the fractional mass of a given lens. Note that $\mathbf{l_i}$ represents the position of the lens normalised by ξ_0. Each lens contributes at least one Type-II image, and at least one Type-I image is always formed as a whole by the collection of lenses. Thus, for 'N' point mass lenses, a minimum of N+1 images are formed. Depending on the position of the source and the lenses, a maximum of 5(N-1) images may be formed ([Asada 09]). While deriving Equation (2.17), the constant ξ_0 is again taken to be the Einstein Radius. In this case, the Einstein Radius is given by $\sqrt{4GM_T D_L D_{LS}/c^2 D_S}$, where $M_T = \Sigma_i M_i$ is the total mass of all the lenses.

Of the different images that are formed, two of them always account for bulk of the magnification. Due to this, |F| oscillates akin to the Isolated Point Mass case, but with one difference: the de-magnified images act as small 'perturbations' to the sinusoidal oscillations, and hence the |F| would appear 'noisy'. Figure 2.6 shows the amplification factor for two values of N. In both cases, values of $\mathbf{l_i}$ have been drawn from a random uniform distribution between -1 and 1. The left panel assumes N = 5, while N = 7 on the right. As can be seen, both the plots showcase an overall sinusoidal behavior, with the de-magnified

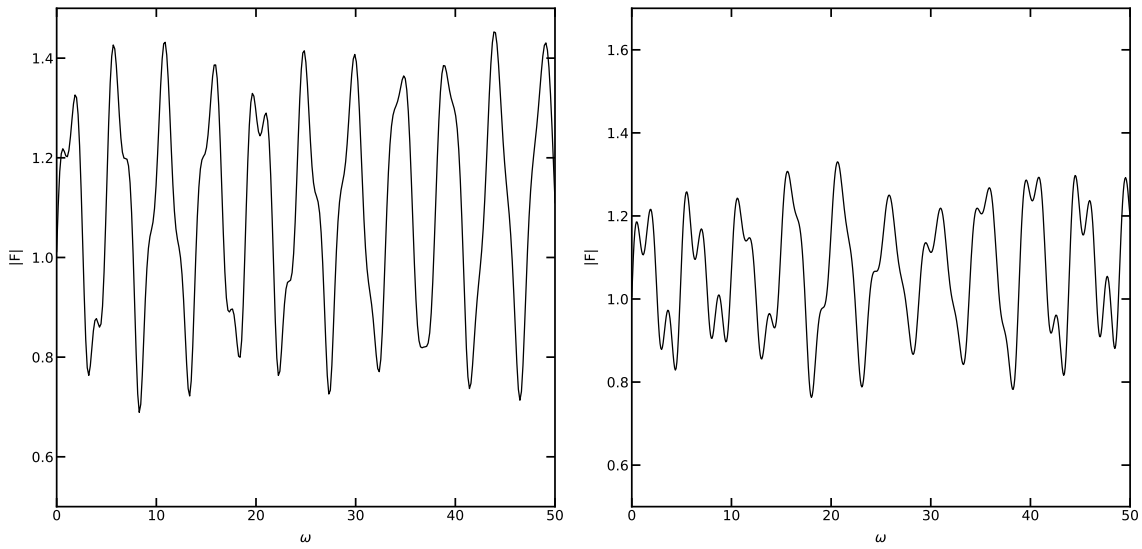

Figure 2.6: Amplification Factor for 'N' point mass lenses on a plane: N = 5 (7) in the left (right) panel. Both plots are as a function of dimensionless frequency $\omega = 8\pi G(1+z_L)M_T f/c^3$.

images accounting for smaller random oscillations. In both panels, |F| has been plotted as a function of $\omega = 8\pi G(1+z_L)M_T f/c^3$.

Chapter 3

Multi-Plane Lensing

In the previous chapter, we had assumed that all lenses under consideration are situated at the same redshift from the observer, i.e on a single lens plane. To generalise this further, we relax the single-plane condition, and explore scenarios wherein lenses may be present at different redshifts. In general, lenses may lie along 'N' lens planes, but as we later show, even something as simple as the two-plane case carries a large number of parameters, and it is not straightforward to make qualitative statements like the previous chapter. We start by extending the equations from Chapter 2 to the multi-plane case, and then explore some possible lens systems for the case of N = 2.

3.1 Formalism of Multi-Plane Lensing

Even in the case of Multi-Plane lensing, the basics remains the same as the single-plane counterpart: the objective is to solve Equation (2.9). The approach is to again consider the incoming radiation as a 2-D wavefront, and propagate it across the lens planes. Doing so, we obtain the following form for the Amplification Factor ([Schneider 92], [Yamamoto 03]):

$$F(f,\mathbf{y}) = Cf^N \int d^2\mathbf{x_1} ... d^2\mathbf{x_N} \exp\left[2\pi i f t_d(\mathbf{x_1},...,\mathbf{x_N},\mathbf{y})\right] \tag{3.1}$$

where, different $\mathbf{x_i}$'s correspond to vectors along the different lens planes, and $\mathbf{x_{N+1}} = \mathbf{y}$. The time delay function is given by $t_d(\mathbf{x_1},...,\mathbf{x_N},\mathbf{y}) = \Sigma_{i=1}^{N} t_d(\mathbf{x_i},\mathbf{x_{i+1}})$, and is now a function of N + 1 variables: the N different vectors along N different lens planes, and the vector along the source plane. C is a factor that depends on the various distances under consideration and is given by $C = \left((\frac{-i}{c})^N \Pi_{i=1}^{N}(1+z_i)\frac{D_{0i}D_{0i+1}}{D_{ii+1}}\right)$. z_i represents the redshift of the i^{th} lens plane, and D_{ij} is the distance between the i^{th} and j^{th} planes, with $i = 0$ $(N+1)$ corresponding to the observer (source plane). As before, the various x_i's correspond to angular distances. Figure 3.1 summarises the lens configuration for N = 2. Note that Equation (3.1) reduces to Equation (2.12) for the special case of N = 1.

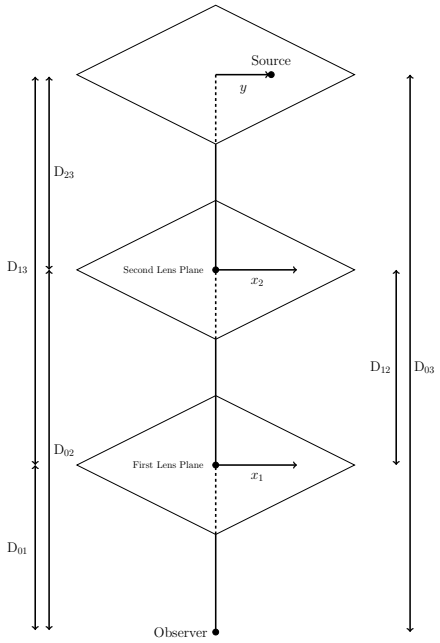

Figure 3.1: Gravitational Lens Configuration. We continue to assume the Thin-Lens Approximation, but now allow lenses to lie on different planes (each corresponding to a unique redshift). For simplicity, the diagram assumes two lens planes, but in general, one could work with N such planes.

Equation (3.1) can be re-written as:

$$\begin{aligned} F(f,\mathbf{y}) = Cf^N \int d^2\mathbf{x_1} \int d^2\mathbf{x_2} \exp\left[2\pi i f t_d(\mathbf{x_1},\mathbf{x_2})\right] \\ \ldots\ldots \\ \ldots\ldots \\ \ldots\ldots \\ \int d^2\mathbf{x_{N-1}} \exp\left[2\pi i f t_d(\mathbf{x_{N-2}},\mathbf{x_{N-1}})\right] \\ \int d^2\mathbf{x_N} \exp\left[2\pi i f t_d(\mathbf{x_N},\mathbf{y})\right] \exp\left[2\pi i f t_d(\mathbf{x_{N-1}},\mathbf{x_N})\right] \end{aligned} \tag{3.2}$$

Going from bottom to top, the result of each integral (more strictly, each *double* integral) is a function of the variable of the next integral (for e.g., the result of the bottom-most integral is a function of $\mathbf{x_{N-1}}$, and so on). We thus cannot break Equation (3.2) into 'N' double integrals while performing the integration numerically. Numerically solving a 2N integral using frequently used quadrature methods is not a very efficient process. Throughout the rest of this chapter, wherever numerical integration of Equation (3.1) is required, we have used a Monte-Carlo Integrator provided by the VEGAS python package ([Lepage 20]). While such a method seems to give reasonable results for the case of N = 2, this too may not be efficient for higher values of N, and one may have to explore alternate options.

3.2 Possible Lens Systems

Similar to the Single-Plane case, Equation (3.1) has to be integrated numerically for all but one case. We begin with the special case for which an analytic expression is available, and later explore other possible scenarios.

3.2.1 The Special Case

Consider a lens arrangement as depicted in Figure 3.2. The position of the source (S) is taken to be the origin. Two Point Mass Lenses are collinear with respect to the source, at (radial) distances r_1 and r_2, with masses M_1 and M_2 respectively. The Observer (O) is present at a distance r_3, and at an angle θ_3 with respect to the source. Due to the symmetry in the Lens configuration, Equation (3.1) can be solved analytically to obtain ([Yamamoto 03]):

$$\begin{aligned} F(k,\theta_3) &= e^{i\alpha} e^{\pi kG(M_1+M_2)/c^2} \Gamma(1-2ikGM_1/c^2)\, z \sum_{L=0}^{\infty} \frac{(-i)^L}{(L!)^2} \Gamma(1+L-2ikGM_2/c^2) \\ &\quad \times (xz)^L {}_2F_1\left(1-2ikGM_1/c^2, 1+L-2ikGM_2/c^2, 1\,; 1-z\right), \end{aligned} \tag{3.3}$$

where,

$$z = \frac{r_3(r_2-r_1)}{r_2(r_3-r_1)}, \tag{3.4}$$

$$x = \frac{kr_2r_3\theta_3^2}{2(r_3-r_2)}. \tag{3.5}$$

α is a real constant corresponding to a constant phase difference, and ${}_2F_1(a,b,c\,;d)$ is the Hypergeometric function. For better visibility, Equation (3.3) has been written in terms of $k = (2\pi f)/c$. Even for this special case, we have six different parameters: r_1, r_2, r_3, M_1, M_2 and θ_3. In the next few plots, we vary these parameters one at a time to provide a qualitative idea about the dependence of the amplification factor on these parameters.

3.2.1.1 Dependence on Radial Distance

In the first set of plots (Figure 3.3), we keep r_3 fixed at 3kpc. In the left (right) panel, we vary the value of $r_1(r_2)$ while keeping $r_2(r_1)$ fixed at 2(2) kpc. We take $M_1 = M_2 = 10M_\odot$, and choose θ_3 such that the observer is at an angle equal to the Einstein Radius when a single point mass lens is kept at 2 kpc , with a total mass of $M_1 + M_2$. Such a choice will allow us to make comparisons with the single plane arrangement that was discussed in Chapter 2.

As the two point masses approach each other (i.e. as $|r_1 - r_2|$ decreases), the amplification factor begins to resemble that of a single point mass lens. This can be seen by

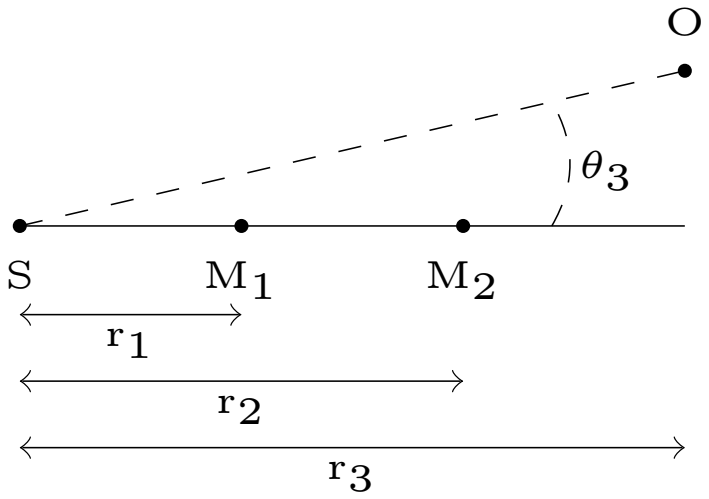

Figure 3.2: Lens Configuration for the Special Case discussed in Section 3.2.1. Two point mass lenses lie collinear with respect to the source.

comparing the black (red) and green curves in the left (right) panel. Thus, differences between the multi-plane and single-plane formalisms become important only when there is a reasonable separation between neighbouring lens planes.

From both panels, there is one more feature that we observe: as either of the lenses move away from the source (or equivalently towards the observer), the oscillations of the |F| curve become more rapid. This is accompanied by a drop in the maximum value that |F| acheives as it oscillates.

3.2.1.2 Dependence on Mass of the Lens

In the next set of plots (Figure 3.4), we keep r_1, r_2, r_3 fixed at $1, 2, 3$ kpc respectively. In the left (right) panel, we vary the value of $M_1(M_2)$ while keeping $M_2(M_1)$ fixed at 10(10) $M_\odot$. For consistency, we again choose θ_3 such that the observer is at an angle equal to the Einstein Radius when a single point mass lens is kept at 2 kpc , with a total mass of $M_1 + M_2$.

As the mass of either of the lenses increases, the oscillations of |F| become more rapid. However, the lens closer to the observer (i.e. M_2) has a greater effect on the rate of oscillations. For example, when (M_1, M_2) = (10, 40) $M_\odot$ (green curve on the left panel), the average period of oscillations is $\sim$ 700 Hz. When we consider the inverse scenario (M_1, M_2) = (40, 10) $M_\odot$ (green curve on the right), the average period is $\sim$ 500 Hz. One can make

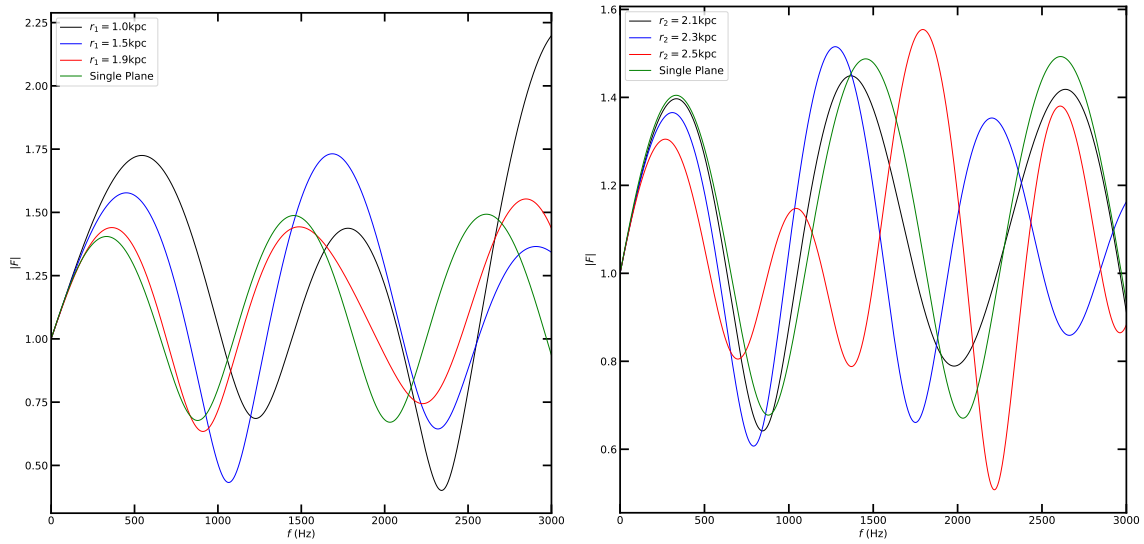

Figure 3.3: Dependence of the amplification factor on radial distance of the two lenses: We fix r_3 = 3kpc, $M_1 = M_2 = 10M_\odot$, and θ_3 = 4.4e-8 rad. In the left panel, we vary r_1 while keeping r_2 fixed at 2 kpc, while r_2 is varied with a fixed value of r_1 = 1 kpc on the right panel.

similar observations by comparing the same-coloured curves from both panels. This is qualitatively similar to the right panel of Figure 2.4.

3.2.1.3 Dependence on θ_3

In this final plot (Figure 3.5), we keep r_1, r_2, r_3 fixed at $1, 2, 3$ kpc respectively, and fix the values of $M_1 = M_2 = 10M_\odot$. We vary the value of θ_3 to understand the effect of this parameter.

Similar to the Single Plane case (left panel of Figure 2.4), as the angular position of the observer approaches the line joining the source with the two lenses, two trends take place: the peak value of |F| increases, and oscillations of |F| become less rapid.

In all the above plots, we have varied only one parameter at a given time. As we show in the next subsection, varying multiple parameters at once produces trends that aren't always a combination of all the above observations.

3.2.2 Relaxing the Collinearity Condition

In this subsection, we relax the condition that requires the two lenses to be collinear with the source. The lens configuration now looks like the one depicted in Figure 3.6. As a result, there are two additional parameters that are to be considered: θ_1 and θ_2. Note that we continue to assume that the source, the observer and the two lenses lie on the same plane (i.e. on the plane of the paper).

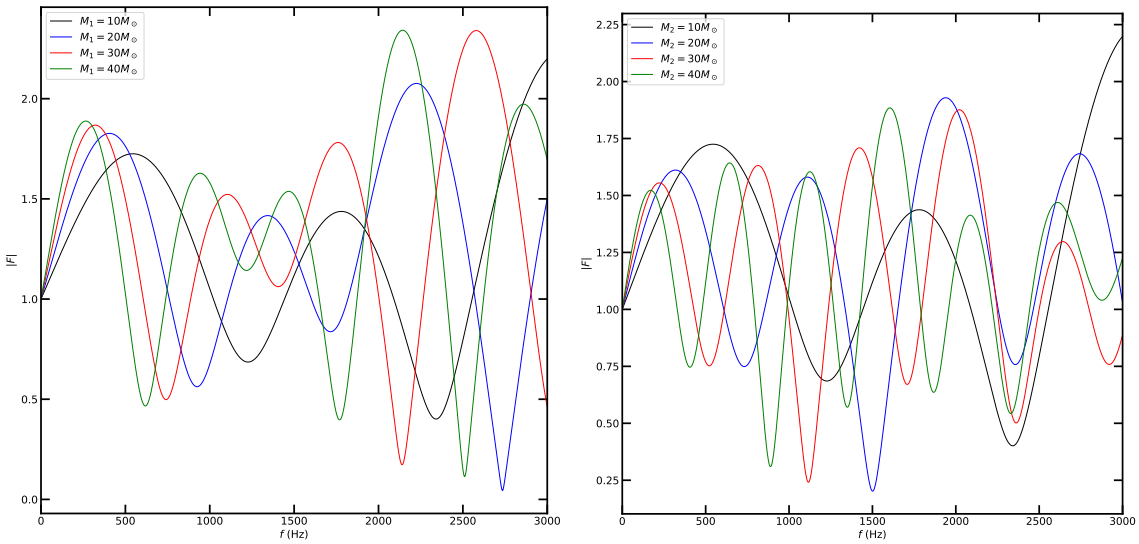

Figure 3.4: Dependence of the amplification factor on the mass of the two lenses: We fix $(r_1, r_2, r_3) = (1,\ 2,\ 3)$ kpc, and θ_3 as described in the main text. In the left panel, we vary M_1 while keeping M_2 fixed at 10 $M_\odot$, while M_2 is varied with a fixed value of $M_1 = 10\ M_\odot$ on the right panel.

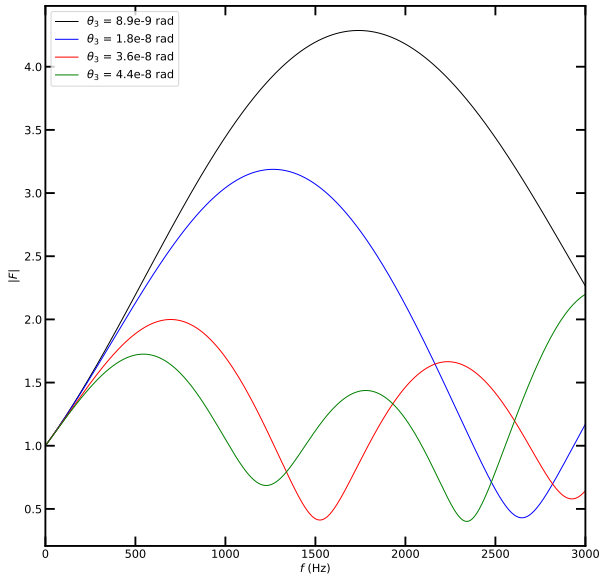

Figure 3.5: Dependence of the amplification factor on the the position of the observer (θ_3): We fix $(r_1, r_2, r_3) = (1,\ 2,\ 3)$ kpc, and $M_1 = M_2 = 10\ M_\odot$. We vary θ_3 by four different factors.

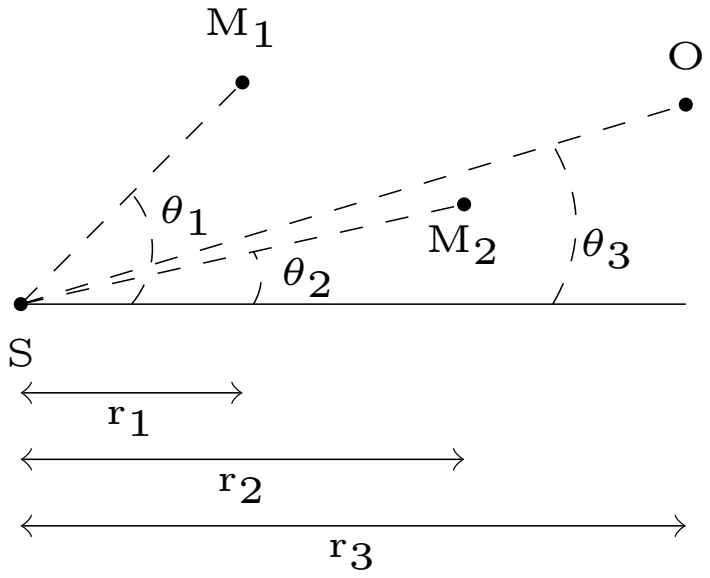

Figure 3.6: Lens Configuration for the Case discussed in Section 3.2.2. The two point masses are no longer collinear with the source.

As has been mentioned earlier, for all plots in this subsection, a Monte-Carlo Integrator provided by the VEGAS python package has been used to numerically integrate Equation (3.1). To verify the accuracy of this method, we first try to reproduce one of the plots that can be made using the analytic expression Equation (3.3). In Figure 3.7, we choose $(r_1, r_2, r_3) = (1, 2, 3)$ kpc, $(M_1, M_2) = (10, 10)\, M_\odot$, and $\theta_3 = 4.4\text{e-}8$ rad, and generate the blue curve using Equation (3.3). The black curve is obtained using numerical integration, and reproduces the analytic expression within an error of 1%. Given the satisfactory accuracy obtained, we proceed to use the same method for all other cases.

We now vary the values of θ_1 and θ_2 while keeping other parameters fixed. We again fix $(r_1, r_2, r_3) = (1, 2, 3)$ kpc, $(M_1, M_2) = (10, 10)\, M_\odot$, and $\theta_3 = 4.4\text{e-}8$ rad. We try four different configurations:

1. $(\theta_1, \theta_2) = (0, 0)$
2. $(\theta_1, \theta_2) = (\frac{2\theta_3}{3}, \frac{-2\theta_3}{3})$
3. $(\theta_1, \theta_2) = (\frac{-2\theta_3}{3}, \frac{-2\theta_3}{3})$
4. $(\theta_1, \theta_2) = (\frac{-2\theta_3}{3}, \frac{2\theta_3}{3})$

Figure 3.8 shows the amplification factor for these four cases. Curves 2 and 3 seem to oscillate at more or less the same rate, and this rate is faster than that of Curve 1. As opposed to this, Curve 4 oscillates slower than Curve 1. This suggests that the angular position of

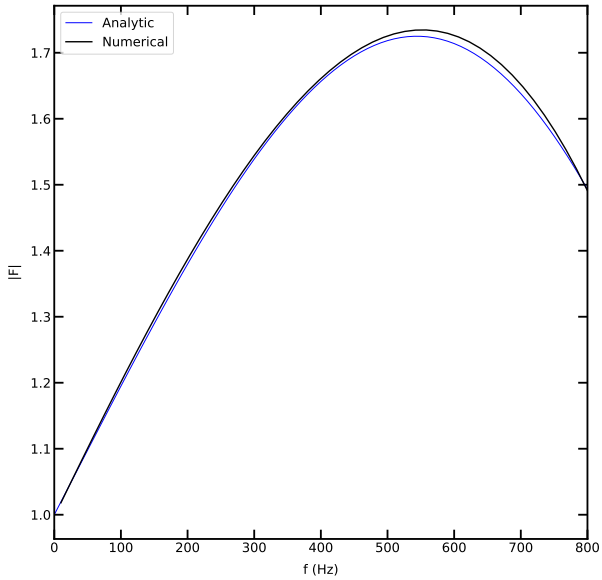

Figure 3.7: Comparing the amplification factor obtained using the Analytic Expression available for the special case (Equation (3.3)) with the one obtained by integrating Equation (3.1) numerically using a Monte-Carlo Integrator.

M_2 has an important effect on the rate of oscillation: as the angular separation between M_2 and the observer decreases, the $|F|$ curve oscillates slower. A comparison between Curve 2 and Curve 3 points towards another trend: When M_1 is closer to the line joining the source with the observer, $|F|$ reaches larger values as it oscillates. Thus, M_1 seems to have a greater effect on magnitude of $|F|$ values, rather than the rate of oscillation.

In Figure 3.9, we fix (M_1, M_2) = (10, 10) $M_\odot$, r_3 = 3 kpc, θ_3 = 4.4e-8 rad, and (θ_1, θ_2) = $(\frac{-2\theta_3}{3}, \frac{2\theta_3}{3})$. One at a time, we vary the values of r_1 and r_2: In both panels, in curve 1, we take (r_1, r_2) = (1, 2) kpc. In the left panel curves 2 and 3 correspond to r_1 = (1.5, 0.5) kpc respectively with r_2 = 2 kpc . In this case, we observe trends similar to the previous section (3.2.1.1) – as M_1 moves away (towards) from the source, the oscillations of the amplification factor become less (more) rapid. On the right panel, for curves 2 and 3, r_2 = (1.5, 2.5) kpc respectively with r_1 = 1 kpc. However, in this case, the observations of Section 3.2.1.1 no longer seem to apply. Thus, the amplification factor in the case of multi-plane lensing seems to have a complicated dependence on the various parameters involved, and it is not always possible to assert monotonous trends for the variation of the different parameters.

We conclude this chapter by noting that the best way to study multi-plane lensing is to select various lens system, and study them case by case, instead of trying to generalize the observations of some test cases.

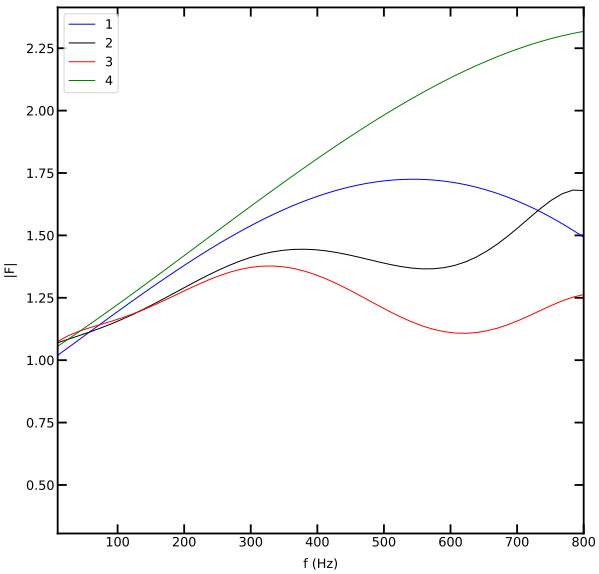

Figure 3.8: Varying the values of θ_1 and θ_2 while keeping $(r_1, r_2, r_3) = (1, 2, 3)$ kpc, (M_1, M_2) = (10, 10) $M_\odot$, and θ_3 = 4.4e-8 rad. The four curves 1, 2, 3 and 4 correspond to (θ_1, θ_2) = (0, 0), $(\frac{2\theta_3}{3}, \frac{-2\theta_3}{3})$, $(\frac{-2\theta_3}{3}, \frac{-2\theta_3}{3})$, $(\frac{-2\theta_3}{3}, \frac{2\theta_3}{3})$ respectively.

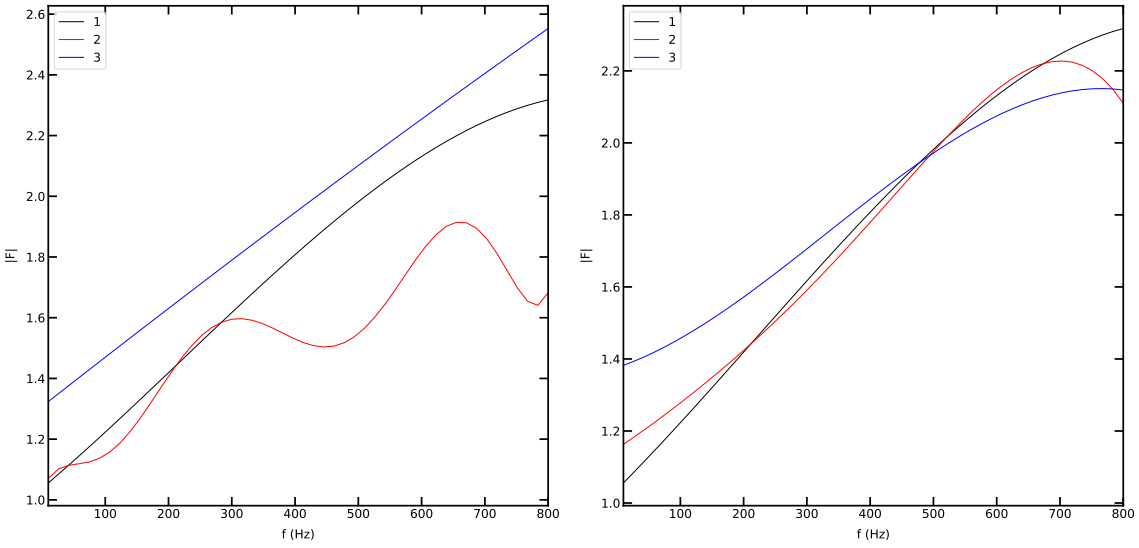

Figure 3.9: Varying r_1 and r_2 while keeping $r_3 = 3$ kpc, $(M_1, M_2) = (10, 10)\ M_\odot$, $\theta_3 = 4.4\text{e-}8$ rad, and $(\theta_1, \theta_2) = (\frac{-2\theta_3}{3}, \frac{2\theta_3}{3})$. In both panels, curve 1 corresponds to (r_1, r_2) = (1, 2) kpc. On the left panel, curves 2 and 3 correspond to r_1 = 1.5 and 0.5 kpc respectively with r_2 = 2 kpc. On the right, we fix r_1 = 1 kpc, with r_2 = 1.5 and 2.5 kpc for curves 2 and 3 respectively.

Chapter 4

Identifying Lensed Gravitational Wave Signals

In this Chapter, we consider cases where gravitational wave signals are lensed. Our aim is to understand the conditions under which signals are strongly distorted by lensing, and to develop a method to identify lensed signals. For initial insights, we begin by considering a Gaussian wave packet as our model signal. We later extend the study to more realistic waveforms. The effect of lensing on the chirp waveform has already been studied in detail (for e.g. [Meena 20]). We here choose to focus on the Gravitational Wave Packet emitted during a Core Collapse Supernova event.

4.1 Gaussian Wave Packets

Owing to it's simplicity, we begin our study by modelling a signal by a Gaussian Wave Packet. Such a waveform is parameterised by two quantities: f_0 and σ_f. The former is the central frequency of the wave packet in frequency domain, while the latter is a measure of the width of the signal, again in frequency domain. Equivalently, one could define analogous quantities t_0 and σ_t in time domain. For a Gaussian Wave Packet, note that $\sigma_t = \frac{1}{2\pi\sigma_f}$. We simulate this signal through the following relation:

$$h(t) = \exp[-0.5((t-t_0)/\sigma_t)^2]\text{Real}\Big(\exp[2\pi\text{if}_0\text{t}]\Big) \tag{4.1}$$

Once simulated, we 'lens' the signal by a model gravitational lens. To do so, we first take a Fourier transform of the signal to obtain the corresponding wave packet in frequency domain $h(f)$. For a given lens system, the lensed wave packet is a product of the wave packet $h(f)$ and the amplification factor F, i.e. $h_L(f) = h(f)F$. The lensed signal in time domain, $h_L(t)$, is obtained by taking an inverse Fourier transform of $h_L(f)$.

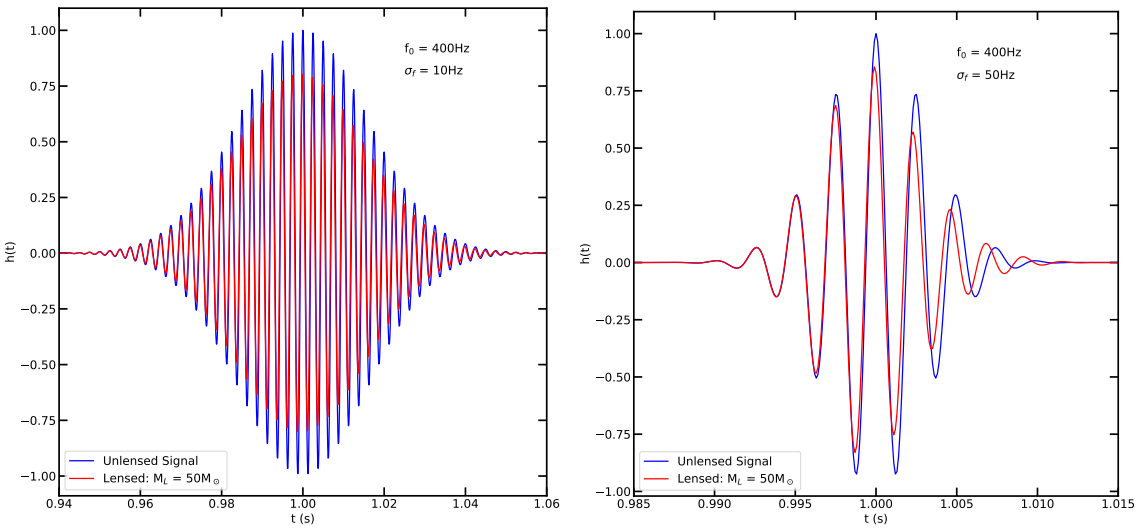

Figure 4.1: Comparison between wide and narrow wave packets. A wide wave packet (in frequency domain) is distorted more.

From hereon, unless otherwise stated, we consider lensing by an isolated point mass with the source situated at $y = 1$. For our model signal, we begin by considering two wave packets that are centred at $f_0 = 400$ Hz, but with different values of σ_f. Figure 4.1 shows these signals – with $\sigma_f = 10$ Hz on the left panel, and $\sigma_f = 50$ Hz on the right panel. Because of the inverse relation between time and frequency domains, the former corresponds to a wide wave packet in time domain, while the latter is narrower. In both cases, the blue curve corresponds to the original signal, while the curve in red is the lensed signal by a $50M_\odot$ lens. Comparison between the two signals in both panels leads to a straightforward observation: a wide signal (in frequency domain) is distorted more in comparison to a narrow signal. One way to understand this to have a look at the amplification factor from Figure 2.3. One could look at either of the panels, i.e. the modulus or the phase of the amplification factor, but we will focus on the former. For a wave packet that is wide in frequency domain, there is a considerable change in the value of the amplification factor across the range of frequencies covered by the signal. For example, a gaussian wave packet extends roughly $3\sigma_f$ across either side of the mean. In our model signal with (f_0, σ_f) = (400, 50) Hz, the amplification factor is as high as ~ 1 at the lower end of the wave packet, dips to a minimum at ~ 400 Hz, and rises to ~ 1.4 towards the higher end of the wave packet. However, for (f_0, σ_f) = (400, 10) Hz, the amplification factor is fairly constant across the frequency range covered by the signal. Thus, wide wave packets experience varied amounts of amplification across their frequency range, and hence are distorted by greater amounts.

From the right panel of Figure 4.1, we see that the signal is not only distorted, but this distortion is asymmetric. An intuitive way to understand the reason for the same is to

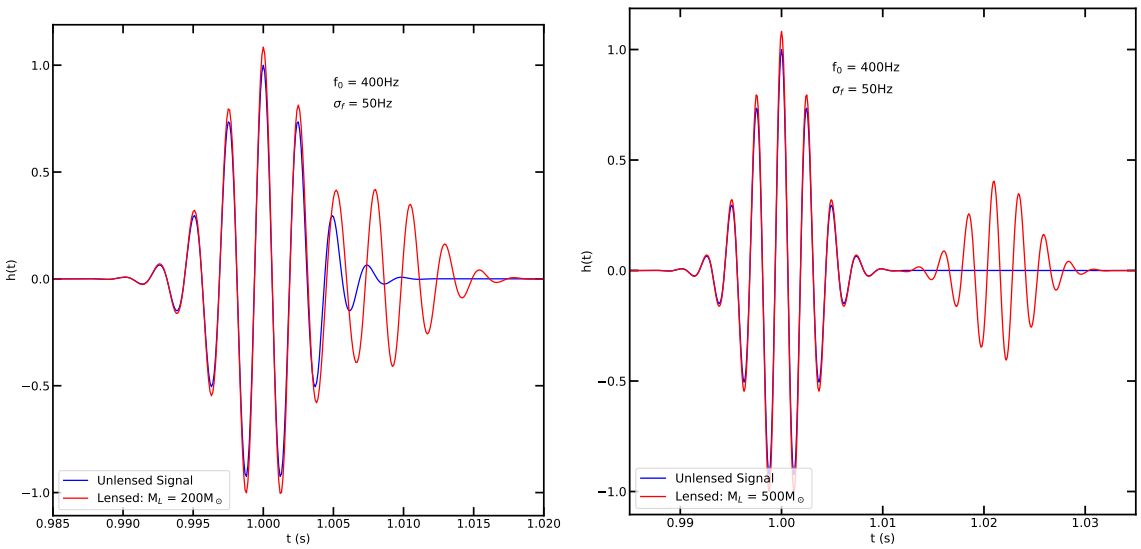

Figure 4.2: Increasing the Mass of the Lens. The lensed signal is a superposition between the all images that are formed.

increase the mass the lens. In Figure 4.2, we fix (f_0, σ_f) = (400, 50) Hz, and assume the mass of the lens to be 200 $M_\odot$ (500 $M_\odot$) in the left (right) panel. On the left panel, we begin to see a non-zero value of the lensed signal in regions where the unlensed signal is absent. On further increasing the mass of the lens, as has been done on the right, we observe two different images. The first image is a Type-I image, and is an enlarged version of the original signal. The image on the right is a Type-II image, and thus has an additional phase difference of $\frac{\pi}{2}$. Thus, a lensed signal is a superposition of the different (diffracted) images that are formed as a result of lensing. Because of the time-delay between the images, the right side of the signal is distorted by a greater extent, and hence the overall distortion of the signal is asymmetric.

4.2 Core Collapse Supernova Gravitational Wave Signal

In the previous section, we had considered a Gaussian Wave Packet as our model signal. In this case, we had a priori knowledge of the shape of the (unlensed) signal, and thus it was straightforward to identify whether a signal has been lensed or not. However, if the shape of the signal is unknown, would it be possible to identify the same? This will be our focus for the rest of the section.

As has already been mentioned in the Introduction, gravitational waves are emitted during core collapse supernovae events. Due to the stochasticity associated with such events, the emitted gravitational wave is noisy. Various computer simulations ([Andresen 17], [Powell 20], [Vartanyan 20], [Yakunin 15], [Yakunin 17], [Morozova 18], [Andresen 19],

[Radice 19], [Warren 20]) have revealed that the signal maintains high intensity only for a short time following the bounce (0.5 to 1 second). In this period, the frequency rises from a few tens of Hertz to slightly over a thousand Hertz. The exact numbers depend on the mass and spin of the progenitor star. Following the bounce, there are various processes that give rise to gravitational waves:

1. f-mode and g-mode oscillations of the Proto-Neutron Star (PNS) give rise to waves in the frequency range of a few hundreds to thousand Hertz. The (relative) intensity of waves produced by this method is the highest.

2. The Standing Accretion Shock Instability (SASI), that is formed as a result of the stalling of the shock by the infalling matter, accounts for waves in the region of $\sim 100-300$ Hz. This is prominent in only those supernovae events where an explosion doesn't take place. Prompt convection following the bounce also gives rise to waves in the same frequency bracket (for the first 10s of milliseconds following the bounce).

3. Asymmetric flow of matter and neutrinos produce waves in the regime of $\sim 0.1-10$ Hz. The strain produced by this is the weakest amongst the various processes highlighted here.

Owing to the randomness associated with the above events, to the best of our knowledge, there are no templates to faithfully reproduce such a signal. However, since we know that the signal is noisy, we have attempted to simulate this signal using a Gaussian Random Field. The wave packet in frequency domain is generated by the following relation:

$$h(f_j) = (a_j + b_j)\sqrt{P(f_j)} \tag{4.2}$$

where, all the a_j's and b_j's are random numbers drawn from a unit Gaussian distribution, and $P(f)$ is the power spectrum. In addition to creating a noisy wave packet, we would like to ensure that the time-evolution of frequency takes up a certain form. To do this, we transition to time domain using the following relation:

$$h(t) = \Sigma_j h(f_j) \exp[-2\pi i f_j t] \tag{4.3}$$

where we, for the time being, take $f_j = f_{0,j} + mt$ – i.e., the frequency increases linearly with a slope m over time.

Figure 4.3 shows one of the realisations of a signal generated using a power spectrum that is random white noise. The left panel is the signal in time domain, the central panel gives the corresponding frequency-time plot. The frequency increases linearly between ~ 100 to ~ 1500 Hz in a span of 0.5 seconds. The right panel is the same signal that has

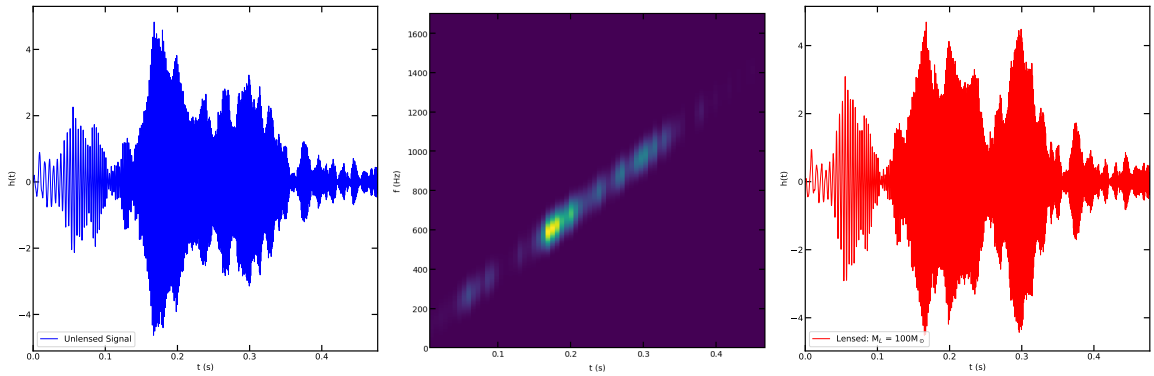

Figure 4.3: Left: A noisy Core Collapse Supernova Gravitational Wave like signal. Centre: The frequency-time plot of the signal. Right: The signal lensed by a $100M_{\odot}$ lens.

been lensed by a $100M_{\odot}$ lens. Comparison between the left-most and right-most panels makes it evident that the unlensed and lensed signals 'look' different. However, since templates for such signals are unavailable at the moment, it is impossible for an observer to identify whether a given signal is lensed just by looking at it.

However, there is a powerful tool that may prove useful in such circumstances: the power spectrum of the signal. To illustrate this point, we show the power spectrum for two cases in Figure 4.4: the left panel considers lensing by a $20M_{\odot}$ lens, while we assume a mass of $100M_{\odot}$ on the right. The curve in blue is the power spectrum of the original signal, red is the power spectrum of the lensed signal, and black is the $|F|$ for the corresponding lenses. Comparison between the red and black curves points towards an interesting trend: the power spectrum of the lensed signal rises and falls in accordance with the oscillations of the amplification factor. For heavier lenses, the amplification factor oscillates at a faster rate, and hence a greater number of these 'alignments' are observed.

While the power spectrum seems to be a useful tool, we would like to know if any statistical inference can be drawn from using such a method. For this, we first generate 100 realisations using a given power spectrum. We next compute the overlap between the amplification factor and the power spectrum by finding the average distance between the peaks of the two curves (for e.g., from Figure 4.4, we compare the blue with the black curve, and the red with the black curve). One could also try to match troughs between the two sets of curves, but these give rise to widely similar results, and we hence focus on peaks alone. To counter the noise of the power spectrum, we use a Savitzky-Golay filter ([Savitzky 64]) to average across 'N' neighbouring bins. The value of 'N' is important, and is to be chosen based on the number of oscillations of the power spectrum. If 'N' is too large (small), one would end up with too few (many) peaks. Once filtered, we locate peaks by comparing neighbouring values to identify local maximas.

Figure 4.5 shows the average distance between peaks of the amplification factor and

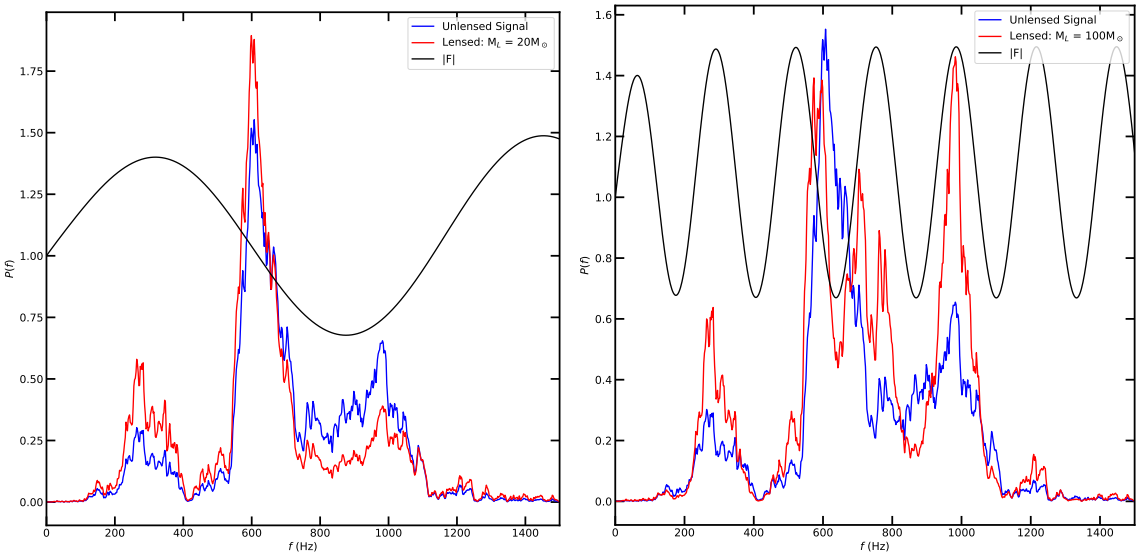

Figure 4.4: Power spectra of Lensed and Unlensed signals from Figure 4.3. The left panel considers a $20M_{\odot}$ lens, and $100M_{\odot}$ on the right.

peaks of the power spectrum using the method explained above. The crosses correspond to median values, while the error bars correspond to the 16^{th} and 84^{th} percentile regions. The data points of the lensed (unlensed) signals is represented by red (blue). The average distance, denoted by Δf, is plotted against M_L, for different lens masses. At relatively low masses, there isn't a big difference between the peak-matching of the unlensed and lensed signals. This is because of the relatively low number of peaks of the amplification factor. As M_L increases, one notices a gradual seperation between the red and blue data points – the probability of identify a lensed signal increases as the signal encounters heavier lenses. While the trend of the red line is as expected, one would expect the median values of the blue curve to 'randomly' oscillate, owing to the intrinsic noise of the signal. However, this too seems to monotonically decrease at high values of M_L. This is due to a limitation of the method we adopt: for higher lens masses, we decrease the value of N for the Savitzky-Golay filter. As a result, a greater number of peaks emerge for the unlensed signal. At a later part of this section, we explore an alternate method to estimate genuine peaks.

While the central frequency increases linearly over time for a Core Collapse Supernova Gravitational Wave Packet, the 'spread' of frequency components varies with time. To simulate such a signal whose frequency evolves like this, we modify Equation (4.3) to:

$$h(t) = \Sigma_{(f_0-3\sigma_f)}^{(f_0+3\sigma_f)} h(f) \exp[-2\pi i f t - (f-f_0)^2/(2\sigma_f^2)]\Delta f \tag{4.4}$$

where, $f_0 \equiv f_0(t)$ is the central frequency, and $\sigma_f \equiv \sigma_f(t)$ is a measure of the spread of the signal (in frequency domain). We choose values such that f_0 increases linearly from 100 Hz to 1000 Hz in a span of 0.4 seconds, and then stabilizes at 1000 Hz for the next

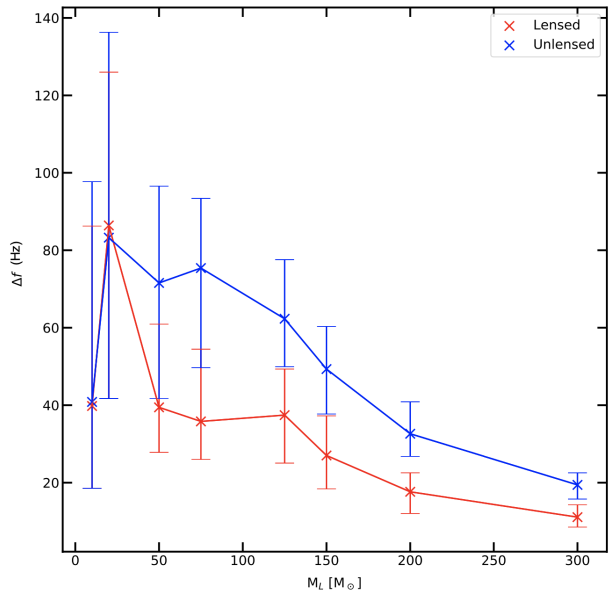

Figure 4.5: Results of the peak finding method for a set of 100 signals simulated using Equation (4.3). The crosses denote median values, while the error bars correspond to the 16^{th} and 84^{th} percentile regions. Points in red (blue) correspond to the lensed (unlensed) signal.

0.1 seconds. σ_f increases linearly from 25 to 100 Hz during the first half of the signal, and drops linearly from 100 to 25 Hz during the second half. One of the realisations of such a signal is shown in the left panel of Figure 4.6, while the corresponding frequency-time plot is shown in the central panel. We simulate hundred such signals and repeat the peak-finding method described above. The results of this is shown on the right panel, and observations remain more or less similar in comparison to Figure 4.5.

While the method used above seems to work well, it suffers from one main drawback – the number of bins used by the Savitzky-Golay filter determines how good the estimation of peaks are, as has been mentioned above. To improve this, we would like to develop a method that better identifies peaks, and ideally is independent of the number of bins used. To do so, we employ the following method: we first use a Savitzky-Golay filter with a bin size of $N = 11$ to smoothen out the power spectrum. For the highest peak of the smoothened power spectrum, we traverse to higher and lower frequencies such that the power is within a fraction x of the power at the peak. We here take $x = 50\%$. The location of the peak is then estimated as a weighted average across the bounded region obtained above: $f_{pk} = \frac{\Sigma P(f) f}{\Sigma P(f)}$. We then repeat this process for all other peaks, selecting peaks in descending order. The left panel of Figure 4.7 gives an example of the peaks estimated by this method for one of the signals simulated using Equation (4.4). In blue is the power spectrum of the signal, in red is what one obtains after using a Savitzky-Golay filter, and the black crosses correspond to the estimated location of peaks. The right panel of the same figure represents the results

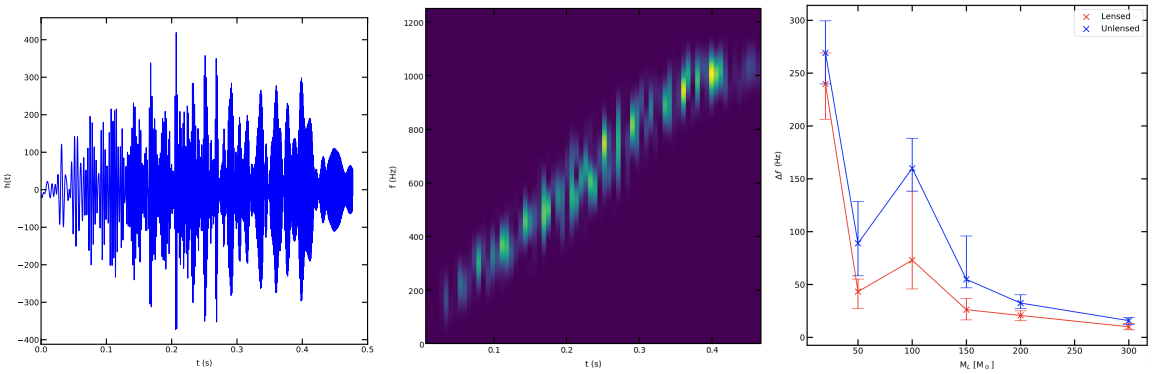

Figure 4.6: Left: One realisation of a signal simulated using Equation (4.4). Centre: The corresponding frequency-time plot. Right: Results of the peak-finding method for 100 such signals. Notations are same as that of Figure 4.5.

of the peak-finding method. One immediately notices a stark difference in results: Unlike Figure 4.5 or Figure 4.6, the median values corresponding to the unlensed signals oscillate randomly, instead of showing a monotonic trend like the lensed values.

Despite the improvement, this method isn't foolproof as well: when one chooses to create a bounded region around each peak such that the power within the region is within 50% of the value of the peak, the number of estimated peaks will remain more or less constant across all signals. As the mass of the lens increases, the number of peaks corresponding to the amplification factor will increase, and at some point, the number of peaks of the amplification factor will equal the number of estimated peaks of the power spectrum. For lens masses above this limit, the value of Δf will appear to worsen due to the limited number of peaks. In such a case, one would have to modify the value of x.

Another way to reduce the number of false peaks would be to consider only those peaks of the smoothened power spectrum that are larger than a given lower threshold (for e.g. three times the rms value). However, introducing such a threshold seems to greatly reduce the number of peaks estimated using our method, and the values of Δf are biased as a result. Introducing such a lower limit would especially be important during real life observations, where detector noise contributes false peaks. We conclude by noting that a more robust method is required to tackle such scenarios.

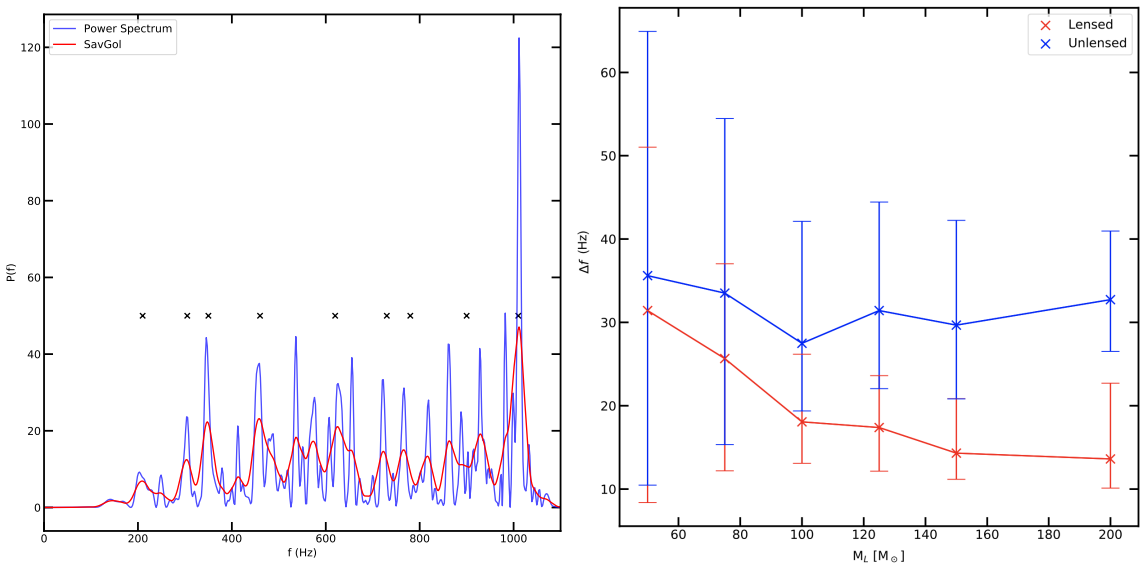

Figure 4.7: Results of the peak finding method using the new weighted average method to estimate the location of peaks. The median values of the unlensed signal oscillate randomly instead of depicting a monotonic trend.

Chapter 5

Summary

In this thesis, we have explored the conditions under which wave effects are important in gravitational lensing – this is when the wavelength of radiation is comparable to the physical size of the lens. For wavelengths much smaller than the lens, geometric optics can be used. At the other extreme, when wavelengths are much larger than the lens, lensing is absent. Equivalently, wave optics is important when the time delay between neighbouring images is comparable to the average time period of oscillation of the incoming radiation.

Gravitational Lensing produces multiple images, and the lensed signal that one observes is a superposition of all these (diffracted) images. When the time delay between images is comparable to the length of the signal in time-domain, distortions are strong in the lensed signal. When one studies a signal whose shape is known, changes produced by lensing may be inferred through a visual inspection of the signal, as long as the intrinsic noise of the detector is small compared to the signal itself. This holds true for waveforms such as the chirp signal, for which various templates are available. However, for a signal like the one produced during a core collapse supernova, it is not easy to predict the shape of the signal. In such a case, it is next to impossible to identify whether a signal has been lensed or not by just looking at the signal. For such a case, it is useful to study the power spectrum of the signal. The power spectrum of a lensed signal shows periodic rises and drops in power in accordance with the oscillations of the amplification factor. This method is, however, useful only for large lenses, for which the amplification factor oscillates multiple times within the frequency range covered by the wave packet.

In addition to studying lensing by a simple model of an isolated point mass lens, we have looked at other possible lensing systems. The simplest of these is that of a point mass lens embedded in an underlying galaxy potential. The effect of the galaxy is to introduce two additional terms into the lensing potential of the point mass lens: convergence and shear. Convergence only increases the magnification and time delay between the images, while shear may additionally increase the number of images in some cases. The next system that

we looked at was that of multiple point mass lenses spread across a single lens plane. The number of images lies between $N+1$ and $5(N-1)$ for $N(>1)$ point mass lenses, but two of these images carry away bulk of the magnification. As a result, the amplification factor exhibits a 'noisy' sinusoidal behavior. All these lens models assumed lenses to be co-planar on a single lens plane. We also looked at the case of multi-plane lensing. Unfortunately, the number of parameters in this case is too large to make generalised statements.

At the moment, there are three detectors that are active as part of the LIGO/VIRGO collaboration. A few more are planned in the form of LIGO-India, the Einstein Observatory, LISA and DECIGO. Some of these detectors will be operational within the next decade or so, and the field of gravitational wave astronomy is expected to rise in significance. Until the present day, over 50 chirp signals have been detected, but none of them have been claimed to be lensed. We wait for the day when improved detectors would allow for the detection of a greater number of gravitational waves, and hope that some of these are lensed during their propagation towards the Earth.

Appendix A

How Good is the Point-Mass Approximation?

Throughout this thesis, we have approximated micro-lenses as point-masses. This may seem acceptable for neutron stars (black holes), whose radii (schwarzschild radii) are often of the order of a few kilometres to a few tens of kilometres. However, stars are much larger objects, with typical radii of the order of 10^6 kilometres. In this section, we aim to explore the conditions under which an object as large as this can be considered as a point-mass.

In what follows, we approximate a star by a uniform-density sphere of radius $R_\star$. The Gravitational Potential is given by:

$$\phi(r) = \begin{cases} -\frac{GM}{2R_\star}(3 - \frac{r^2}{R_\star^2}) & ;r \leq R_\star \\ -\frac{GM}{R_\star} & ;r \geq R_\star \end{cases} \tag{A.1}$$

The lensing potential can then be written as ([Suyama 05]):

$$\psi(x) = \begin{cases} \ln[1 + (1 - (x/R)^2)^{0.5}] - (1/3)[4 - (x/R)^2][1 - (x/R)]^{0.5} & ;x \leq R \\ \ln[x/R] & ;x \geq R \end{cases} \tag{A.2}$$

where, $R = R_\star/\xi_0$ is the radius of the star normalised by the Einstein Radius of the Lens system. As it turns out, the parameter R is what determines the accuracy of this approximation.

Figure A.1 shows the (modulus of the) Amplification factor obtained by using the above lensing potential (in black). The left panel assumes a value of $R = 0.1$, while $R = 1$ on the right panel. In blue, the amplification factor of a point mass lens is provided for reference. We readily see that for $R = 0.1$, the point mass approximation almost reproduces the black curve perfectly. In fact, this holds true $R \leq (0.4 - 0.5)$. For larger values of R, we begin seeing discrepancies between the two curves, and the point mass approximation no longer holds.

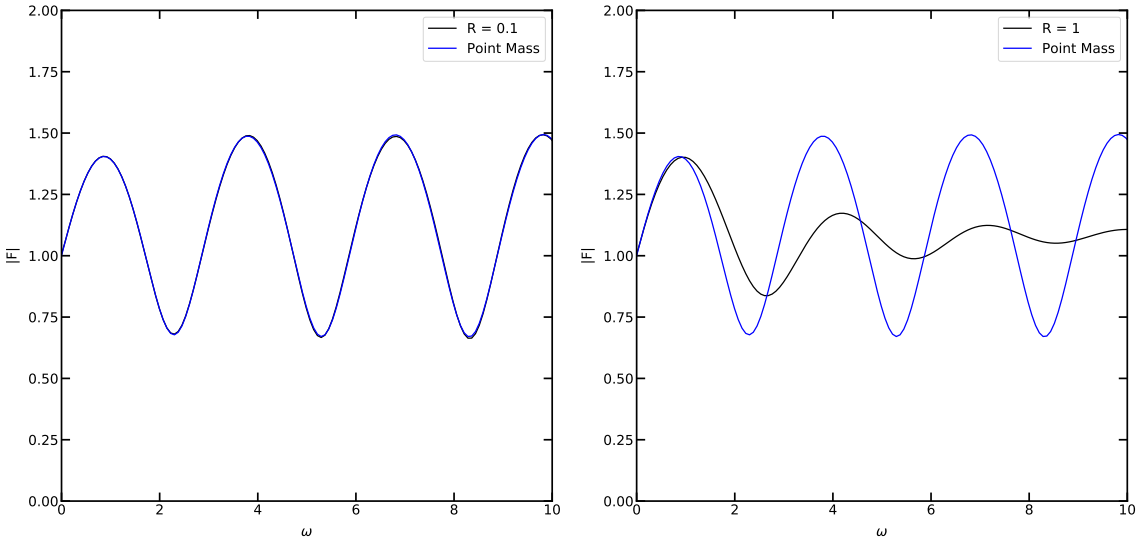

Figure A.1: Amplification Factor for a Lens approximated as a Uniform Density Sphere (in black) (as a function of dimensionless frequency, $\omega = 8\pi G(1+z_L)M_L f/c^3$). Left Panel: $R = 0.1$; Right Panel: $R = 1$. For reference, the amplification factor of a Point Mass Lens (for the same lens/source parameters) is shown in blue.

To assess the physical situations during which the point mass approximation holds, we next provide certain ballpark numbers for the value of R:

1. For a lens system in which all distances are of the order of one kpc, and for a solar mass lens, the Einstein radius is of the order of 10^{-9} rad. The angular size of the sun at this distance is $\sim 10^{-11}$ rad, and thus $R \sim 0.01$. For typical galactic distances, a solar mass star is well approximated by a point mass.

2. For stars on the Main Sequence, $R_\star \propto M^{0.57}$ (for e.g. [Eker 18]), while the Einstein radius $\propto M^{0.5}$. Thus, $R \propto M^{0.07}$. The value of R remains fairly constant with increase in mass, and hence the point mass approximation holds true for even larger stars within typical galactic distances.

3. For a general distance D, the Einstein Radius $\propto \sqrt{D}$, while the angular size of an object $\propto D^{-1}$, and hence $R \propto \frac{1}{\sqrt{D}}$. At large values of D ($>$ 1kpc), the value of R is bound to decrease. However, for values of $D < 1kpc$, the value of R will begin to increase, and if D happens to be a few parsecs, R will be of order unity. It is only in this unlikely scenario when the point mass approximation does not hold for a star.

Given that the uniform sphere model is a highly simplified and unrealistic model, one may try to use an alternate mass distribution. One possibility is that of a polytrope of index $n = 3$, but as has been shown in the past ([Ohanian 74]), the difference is noticeable only when $R \sim 1$.

Appendix B

The Ulmer-Goodman Formalism

The Ulmer-Goodman formalism [Ulmer 95] is a method to compute the amplification factor in time-domain in lieu of frequency-domain. Equation (2.12) in time-domain is:

$$F(t,\mathbf{y}) = \int_{-\infty}^{\infty} dfF(f,\mathbf{y}) \exp(-2\pi i f t) = \int d^2\mathbf{x}\, \delta[t_d(\mathbf{x},\mathbf{y}) - t] \tag{B.1}$$

The estimation of $F(t,\mathbf{y})$ is thus reduced to a line integral over contours with $t_d(\mathbf{x},\mathbf{y}) = t$. Transiting from time to frequency domain (or the inverse) can be performed using the ever efficient FFT algorithm ([Cooley 65]), and thus computation of (2.12) is much faster even for a general lens system of 'N' lenses on a single lens plane.

Unfortunately, extending this formalism to a Multi-Lens Plane scenario is accompanied by a fair share of challenges. In this case,

$$F(t,\mathbf{y}) = \int_{-\infty}^{\infty} dfF(f,\mathbf{y}) \exp(-2\pi i f t) = \int d^2\mathbf{x_1} ... d^2\mathbf{x_N} \delta[t_d(\mathbf{x_1},...,\mathbf{x_N},\mathbf{y}) - t] \tag{B.2}$$

For a general case of N lens-planes, points lying on a higher-dimensional contour ($t_d(\mathbf{x_1},...,\mathbf{x_N},\mathbf{y}) = t$) would contribute to $F(t,\mathbf{y})$. At the moment, to the best of our knowledge, there happens to be no efficient method to estimate such high-dimensional contours.

One possible alternative is to 'freeze' values for all but one set of variables, use (an analogue of) Equation (B.1), and iterate over all other variables to obtain Equation (B.2). If each iterate takes T amount of time to compute, then the total time this method would take is $Tm^{2(N-1)}$, where m is the grid size (used to define the various $\mathbf{x_i}$'s) employed. T is usually of the order of minutes to hours, while m is usually of the order of 10^3. Unfortunately, even for $N = 2$, this seems to be very inefficient.

Although the Ulmer-Goodman formalism is extremely useful for the case of Single-Plane lensing, an alternate method is required for the Multi-Plane counterpart.

Appendix C

Wave Packet Succeeding a Chirp Signal

During the in-spiral process between two massive objects, a 'chirp signal' is emitted. At the moment of coalescence, a gravitational wave packet is emitted. Figure C.1 provides an example of these signals for a $1M_{\odot} + 1M_{\odot}$ binary system. We have simulated these signals using the PyCBC package ([Nitz 21]). The left panel shows the chirp signal produced during the final ~ 0.1 seconds before coalescence, while the wave packet is shown on the right. For the binary system considered here, the wave packet is only ~ 0.5 milliseconds long.

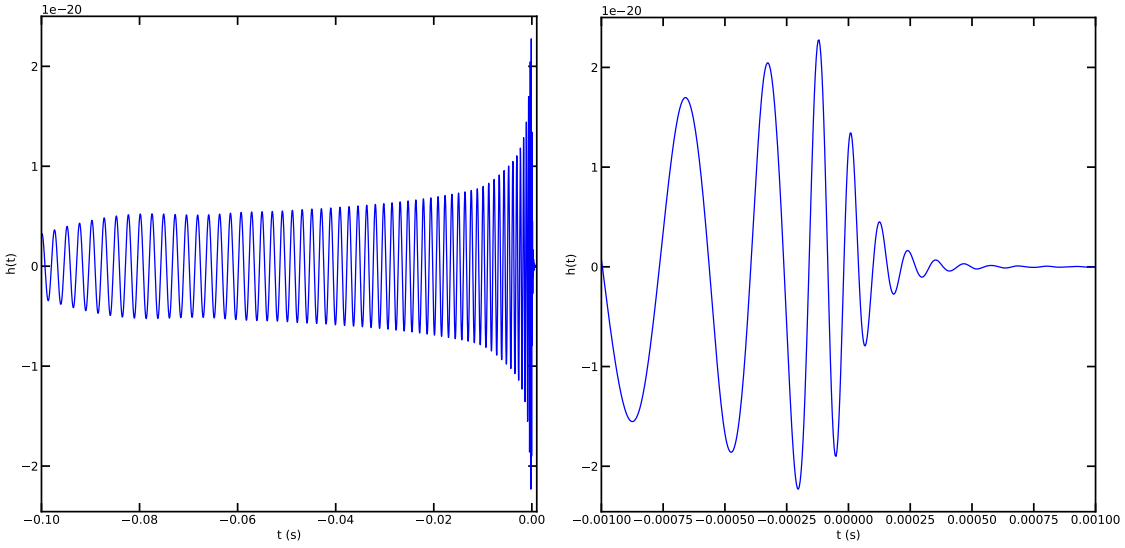

Figure C.1: A gravitational wave signal produced during the inspiral of a $1M_{\odot} + 1M_{\odot}$ binary system. The well-known chirp signal is shown on the left, while the wave packet is shown on the right.

Unlike all the cases that have been discussed in this thesis, the wave packet is not 'isolated', but is rather attached to the chirp signal that precedes it. Due to this, it is not easy to observe multiple distinct images of the wave packet. Figure C.2 portrays how the above

wave packet would appear if it is lensed by $10M_\odot$ lens (left) and $30M_\odot$ lens (right). Here, we have again assumed an isolated point mass lens. Even though the wave packet appears visually different, it may not always be easy to identify this difference during real life observations, for two reasons: the time resolution of the detector may not allow such fine measurements, and/or the detector noise may limit observations.

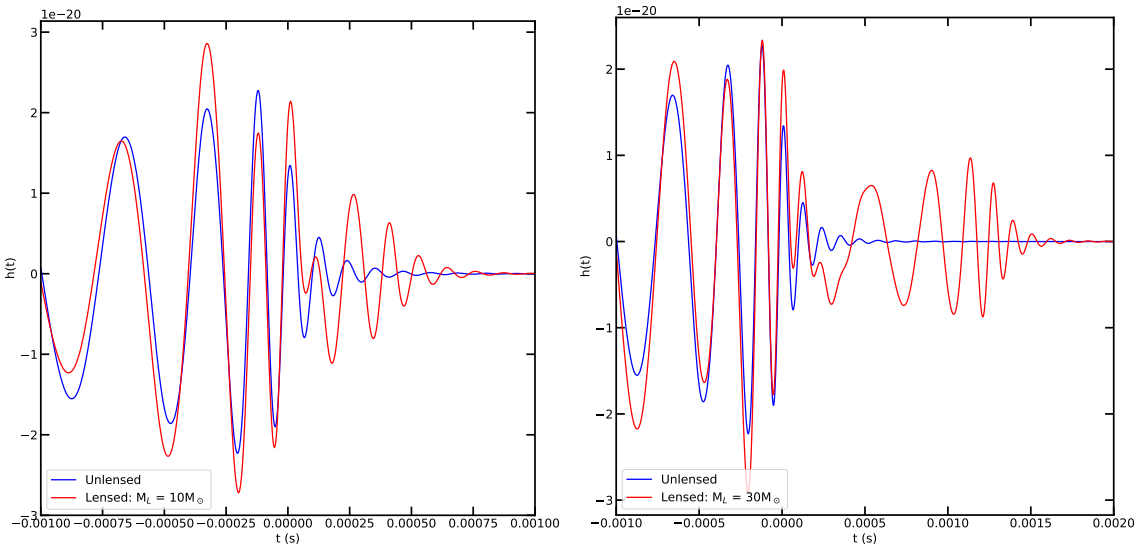

Figure C.2: Lensing of the above wave packet by a $10M_\odot$ lens (left) and $30M_\odot$ lens (right).

Suppose such measurements are made at some point in the future, there is an important application that can envisaged: if both the source and lens happen to be extragalactic, the galaxy in which the micro-lens is situated will lens the signal as well. The time delay caused by the galaxy lens can be as large as a few days, so distinct signals will be observed in such a case. Each of these images would further be lensed by any micro-lenses in their vicinity, which would impart features such as those shown in Figure C.2. If macro-images are obeserved within a few days of each other, these minute features caused by the micro-lens may help decide if the different signals are indeed macro-images, or signals emitted by different sources.

Bibliography

[Andresen 17] H. Andresen, B. Müller, E. Müller & H. Th. Janka. *Gravitational wave signals from 3D neutrino hydrodynamics simulations of core-collapse supernovae*. , vol. 468, no. 2, pages 2032–2051, June 2017.

[Andresen 19] H Andresen, E Müller, H-Th Janka, A Summa, K Gill & M Zanolin. *Gravitational waves from 3D core-collapse supernova models: The impact of moderate progenitor rotation*. Monthly Notices of the Royal Astronomical Society, vol. 486, no. 2, page 2238–2253, Apr 2019.

[Asada 09] H. Asada. *Perturbation theory ofNpoint-mass gravitational lens systems without symmetry: small mass-ratio approximation*. Monthly Notices of the Royal Astronomical Society, vol. 394, no. 2, page 818–830, Apr 2009.

[Baraldo 99] Christian Baraldo, Akio Hosoya & Takahiro T. Nakamura. *Gravitationally induced interference of gravitational waves by a rotating massive object*. Phys. Rev. D, vol. 59, page 083001, Mar 1999.

[Collaboration 16] LIGO Scientific Collaboration & Virgo Collaboration. *Observation of Gravitational Waves from a Binary Black Hole Merger*. Phys. Rev. Lett., vol. 116, page 061102, Feb 2016.

[Cooley 65] J. Cooley & J. W. Tukey. *An algorithm for the machine calculation of complex Fourier series*. Mathematics of Computation, vol. 19, pages 297–301, 1965.

[Eker 18] Z Eker, V Bakış, S Bilir, F Soydugan, I Steer, E Soydugan, H Bakış, F Aliçavuş, G Aslan & M Alpsoy. *Interrelated main-sequence mass–luminosity, mass–radius, and mass–effective temperature relations*. Monthly Notices of the Royal Astronomical Society, vol. 479, no. 4, page 5491–5511, Jul 2018.

[Lepage 20] G. Peter Lepage. *Adaptive Multidimensional Integration: VEGAS Enhanced*, 2020.

[Meena 20] Ashish Kumar Meena & Jasjeet Singh Bagla. *Gravitational lensing of gravitational waves: wave nature and prospects for detection*. , vol. 492, no. 1, pages 1127–1134, February 2020.

[Misner 73] Charles W. Misner, K. S. Thorne & J. A. Wheeler. Gravitation. W. H. Freeman, San Francisco, 1973.

[Morozova 18] Viktoriya Morozova, David Radice, Adam Burrows & David Vartanyan. *The Gravitational Wave Signal from Core-collapse Supernovae*. The Astrophysical Journal, vol. 861, no. 1, page 10, Jun 2018.

[Nakamura 99] T. T. Nakamura & S. Deguchi. *Wave Optics in Gravitational Lensing*. Progress of Theoretical Physics Supplement, vol. 133, pages 137–153, January 1999.

[Narayan 96] Ramesh Narayan & Matthias Bartelmann. *Lectures on gravitational lensing*. arXiv preprint astro-ph/9606001, 1996.

[Nitz 21] Alex Nitz, Ian Harry, Duncan Brown, Christopher M. Biwer, Josh Willis, Tito Dal Canton, Collin Capano, Larne Pekowsky, Thomas Dent, Andrew R. Williamson, Gareth S Davies, Soumi De, Miriam Cabero, Bernd Machenschalk, Prayush Kumar, Steven Reyes, Duncan Macleod, dfinstad, Francesco Pannarale, Thomas Massinger, Sumit Kumar, Márton Tápai, Leo Singer, Sebastian Khan, Stephen Fairhurst, Alex Nielsen, Shashwat Singh & Bhooshan Uday Varsha Gadre. *gwastro/pycbc: 1.18.0 release of PyCBC*, February 2021.

[Ohanian 74] Hans C. Ohanian. *On the Focusing of Gravitational Radiation*. International Journal of Theoretical Physics, vol. 9, no. 6, pages 425–437, June 1974.

[Peters 74] P. C. Peters. *Index of refraction for scalar, electromagnetic, and gravitational waves in weak gravitational fields*. Phys. Rev. D, vol. 9, pages 2207–2218, 1974.

[Powell 20] Jade Powell & Bernhard Müller. *Three-dimensional core-collapse supernova simulations of massive and rotating progenitors*. , vol. 494, no. 4, pages 4665–4675, June 2020.

[Radice 19] David Radice, Viktoriya Morozova, Adam Burrows, David Vartanyan & Hiroki Nagakura. *Characterizing the Gravitational Wave Signal from Core-collapse Supernovae*. The Astrophysical Journal, vol. 876, no. 1, page L9, Apr 2019.

[Savitzky 64] Abraham Savitzky & Marcel JE Golay. *Smoothing and differentiation of data by simplified least squares procedures.* Analytical chemistry, vol. 36, no. 8, pages 1627–1639, 1964.

[Schneider 92] Peter Schneider, Jürgen Ehlers & Emilio E. Falco. Gravitational Lenses. 1992.

[Shapiro 64] Irwin I Shapiro. *Fourth test of general relativity*. Physical Review Letters, vol. 13, no. 26, page 789, 1964.

[Suyama 05] Teruaki Suyama, Ryuichi Takahashi & Shugo Michikoshi. *Wave propagation in a weak gravitational field and the validity of the thin lens approximation*. Physical Review D, vol. 72, no. 4, Aug 2005.

[Ulmer 95] Andrew Ulmer & Jeremy Goodman. *Femtolensing: Beyond the semi-classical approximation*. The Astrophysical Journal, vol. 442, page 67, Mar 1995.

[Vartanyan 20] David Vartanyan & Adam Burrows. *Gravitational Waves from Neutrino Emission Asymmetries in Core-collapse Supernovae*. The Astrophysical Journal, vol. 901, no. 2, page 108, Sep 2020.

[Warren 20] MacKenzie L. Warren, Sean M. Couch, Evan P. O'Connor & Viktoriya Morozova. *Constraining Properties of the Next Nearby Core-collapse Supernova with Multimessenger Signals*. The Astrophysical Journal, vol. 898, no. 2, page 139, Jul 2020.

[Yakunin 15] Konstantin N. Yakunin, Anthony Mezzacappa, Pedro Marronetti, Shin'ichirou Yoshida, Stephen W. Bruenn, W. Raphael Hix, Eric J. Lentz, O. E. Bronson Messer, J. Austin Harris, Eirik Endeve, John M. Blondin & Eric J. Lingerfelt. *Gravitational Wave Signatures of Ab Initio Two-Dimensional Core Collapse Supernova Explosion Models for 12-25 Solar Masses Stars*, 2015.

[Yakunin 17] Konstantin N. Yakunin, Anthony Mezzacappa, Pedro Marronetti, Eric J. Lentz, Stephen W. Bruenn, W. Raphael Hix, O. E. Bronson

Messer, Eirik Endeve, John M. Blondin & J. Austin Harris. *The Gravitational Wave Signal of a Core Collapse Supernova Explosion of a $15M_{\odot}$ Star*, 2017.

[Yamamoto 03] Kazuhiro Yamamoto. *Path Integral Formulation for Wave Effect in Multi-lens System*. arXiv e-prints, pages astro–ph/0309696, September 2003.